Necking and failure of constrained 3D microtissues induced by cellular tension

Hailong Wang[a], Alexander A. Svoronos[b], Thomas Boudou[c], Mahmut Selman Sakar[d], Jacquelyn Youssef Schell[b], Jeffrey R. Morgan[b], Christopher S. Chen[c], and Vivek B. Shenoy[a,1]

[a]Department of Materials Science and Engineering and [c]Department of Bioengineering, University of Pennsylvania, Philadelphia, PA 19104; [b]Department of Molecular Pharmacology, Physiology, and Biotechnology, Center for Biomedical Engineering, Brown University, Providence, RI 02912; and [d]Institute of Robotics and Intelligent Systems, Eidgenössische Technische Hochschule Zürich, CH 8092 Zurich, Switzerland

Edited by David A. Weitz, Harvard University, Cambridge, MA, and approved November 15, 2013 (received for review July 24, 2013)

In this paper we report a fundamental morphological instability of constrained 3D microtissues induced by positive chemomechanical feedback between actomyosin-driven contraction and the mechanical stresses arising from the constraints. Using a 3D model for mechanotransduction we find that perturbations in the shape of contractile tissues grow in an unstable manner leading to formation of "necks" that lead to the failure of the tissue by narrowing and subsequent elongation. The magnitude of the instability is shown to be determined by the level of active contractile strain, the stiffness of the extracellular matrix, and the components of the tissue that act in parallel with the active component and the stiffness of the boundaries that constrain the tissue. A phase diagram that demarcates stable and unstable behavior of 3D tissues as a function of these material parameters is derived. The predictions of our model are verified by analyzing the necking and failure of normal human fibroblast tissue constrained in a loop-ended dog-bone geometry and cardiac microtissues constrained between microcantilevers. By analyzing the time evolution of the morphology of the constrained tissues we have quantitatively determined the chemomechanical coupling parameters that characterize the generation of active stresses in these tissues. More generally, the analytical and numerical methods we have developed provide a quantitative framework to study how contractility can influence tissue morphology in complex 3D environments such as morphogenesis and organogenesis.

tissue mechanics | tissue remodeling

Cytoskeletal tension is fundamental to many cellular processes such as cell motility (1), cytokinesis (2), tissue morphogenesis (3–6), and remodeling, as well as pathologic processes such as tumor growth, metastasis (7), and fibrosis (8). Moreover, it is becoming increasingly clear that tissue-engineering strategies can benefit from a fundamental understanding of cytoskeletal tension (3–6). A number of cells such as fibroblasts, cardiomyocytes, epithelial cells, endothelial cells, and smooth muscle cells develop significant contractile forces as part of their physiological function (9–12). One important function of cellular forces is to act on the surrounding extracellular matrix (ECM), align the matrix, and reorganize tissues as they form and develop. Most biological tissues experience multiaxial loading in vivo, often with complex boundary constraints. The mechanical stresses that arise from these constraints will lead to spatial variations in contractility, which in turn can influence the morphology of the tissue.

To quantitatively study the influence of mechanical constraints and matrix stiffness on contractility, we have recently developed a microelectromechanical systems-based technology to generate arrays of microtissues embedded within 3D micropatterned matrices that mimic the biomechanical environment that cells see in a native tissue. In our experiments, microcantilevers simultaneously constrain contraction of cardiac microtissues (CMTs) and report forces generated by the CMTs in real time (Fig. 1). Depending on the stiffness of the cantilevers and the density of the collagen matrix, the tissue was found to either fail by thinning and necking at the center or attain a stable, yet significantly strained morphology (6).

It has also been demonstrated that monodispersed cells can organize themselves into 3D microtissues in the absence of an ECM or scaffold (3, 4, 13, 14). To examine the role of mechanical constraints on contractility and morphology of these microtissues, building on the method to form complex shapes (3, 4), here we designed hydrogel molds to consistently control the generation of tension and failure spatially. The molds consisted of recesses in the shape of two toroids connected by a central trough, thus forming a loop-ended dog bone (Fig. 2). When fibroblasts settled into the recess bottoms and began self-assembling, the resulting dog bones were constrained by and suspended between the recessed pegs. The connecting rod between the pegs narrowed significantly, ultimately failing in the middle, leaving two tori microtissues. Furthermore we found that treating the cells with Y-27632 (3), a well-known inhibitor of Rho kinase-mediated contraction, led to tissues that were stable against necking, while treating the tissues with TGF-β led to more rapid narrowing and failure compared with untreated controls. These observations clearly show that the intrinsic contractility of microtissues in constrained geometries leads to morphological instabilities that are strong enough to cause failure of the tissues.

Why do constrained microtissues narrow and fail catastrophically? And, why does failure depend on the stiffness of the boundaries and the density of the matrix? Answers to these questions can help us understand how tissues regulate their contractility temporally and spatially in response to mechanical cues. In this paper, we develop a quantitative framework to model morphological evolution and failure in 3D microtissues and derive a criterion to determine the stable and unstable behavior as a function of

Significance

Tension generated by molecular motors is fundamental to many processes such as cell motility, tissue morphogenesis, tumor growth, metastasis, and fibrosis. Cell-derived tension depends strongly on the mechanical environment. The rigidity of the medium in which the cells are found has been shown to affect cell division, differentiation, and apoptosis. In this work, through a combination of experiments and mathematical models, we find that cell-derived tension can be of sufficient magnitude to cause failure of complex-shaped microtissues. We show that failure can be controlled by varying the amount of extracellular matrix in the tissue and by tuning the stiffness of the constraining structures. Our results can aid the design of stable tissue constructs for applications in regenerative medicine.

Author contributions: V.B.S. designed research; H.W., A.A.S., T.B., M.S.S., J.Y.S., and V.B.S. performed research; J.R.M. and C.S.C. contributed new reagents/analytic tools; H.W., A.A.S., T.B., J.R.M., C.S.C., and V.B.S. analyzed data; and V.B.S. wrote the paper.

The authors declare no conflict of interest.

This article is a PNAS Direct Submission.

[1]To whom correspondence should be addressed. E-mail: vshenoy@seas.upenn.edu.

This article contains supporting information online at www.pnas.org/lookup/suppl/doi:10.1073/pnas.1313662110/-/DCSupplemental.

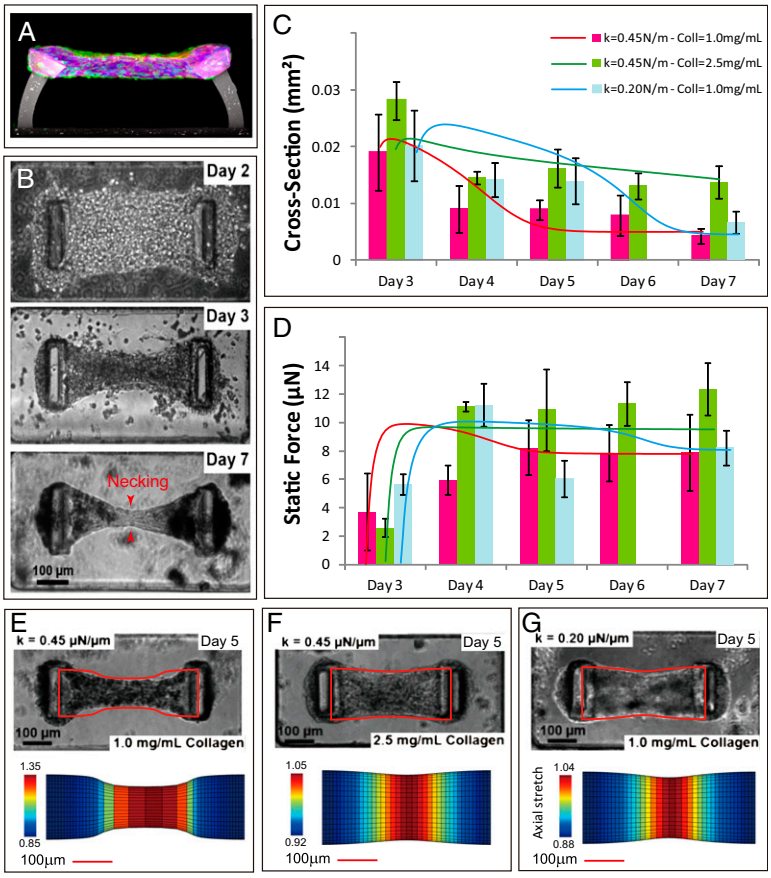

Fig. 1. Influence of microcantilever stiffness and matrix composition on static contractility and the cross-sectional area of CMTs. (*A*) Side view showing a linear band of CMT held by cantilevers. (*B*) Temporal evolution of CMTs constructed in 0.5 mg/mL fibrin and 1.0 mg/mL collagen gels and tethered to rigid (k = 0.45 mN/mm) cantilevers. Shown are representative images depicting the time course of contracting CMTs. Red arrowheads indicate the locations of necking and failure at day 7. (*C*) Cross-sectional area and (*D*) force evolution for various pillar stiffnesses and collagen densities. The bar charts with error bars (standard deviations of 20 CMTs) represent experimental observations, while the curves are fits from simulations. (*E*–*G*) Contracted morphology of tissues with different pillar stiffnesses: (*Upper*) experimental observations along with the shapes from simulations and (*Lower*) finite element mesh showing relative stretch ratios along the tissue.

geometric and biochemomechanical material parameters. We show that stress-dependent active contraction gives rise to a unique type of necking instability that is distinct from other elastic instabilities hitherto studied. By comparing the observed morphologies with the predictions of our model, we are able to determine the chemomechanical material parameters that govern active response in different types of tissues.

Experiments on 3D Microtissue Constructs

Mechanics and Stability of Engineered Cardiac Tissues. To examine the role of mechanical constraints on dynamic contractility and morphology of engineered cardiac tissues, we generated microscale constructs of cardiac cells within collagen/fibrin 3D matrices in microfabricated arrays of wells within a polydimethylsiloxane (PDMS) mold as described previously (6). Two T-shaped cantilevers incorporated within each template constrained the contracting matrix to form a linear band that spanned across the top of the pair of cantilevers (Fig. 1*A*). The spring constant of each cantilever could be controlled by altering the ratio between PDMS and curing agent, whereas the mechanical properties of the ECM could be modulated by varying the collagen density. Remodeling and compaction of the matrix by the cells led to a steady reduction of construct size (Fig. 1*B*), while the contractility of the CMTs increased, leading also to thinning at the center of the linear band between the cantilevers. By day 7, the width of the tapered central part of the tissue was significantly smaller than the rest of the tissue, subsequently leading to failure.

Interestingly, the density of the collagen/fibrin matrix impacted both the shape and the cross-sectional area of the tissue, as well the tensile force it exerted on the cantilevers. We observed that the tension increased when the collagen density was increased from 1.0 to 2.5 mg/mL (Fig. 1*D*), reaching plateau values of 8.0 ± 2.2 and 11.4 ± 1.7 μN, respectively. However, this higher tension in the CMTs constructed from 2.5 mg/mL collagen was not sufficient to overcome the increased rigidity of the denser collagen matrix, thus leading to better stability against necking (Fig. 1*F*). In addition to the density of the ECM we examined the influence of the spring constant of the cantilevers. The static tension was higher between flexible cantilevers (k = 0.20 N/m) than CMTs between rigid cantilevers (k = 0.45 N/m) at day 4 (Fig. 1*D*). Nevertheless, the significantly lower beating contractility of the CMTs tethered to flexible cantilevers (Fig. 1*G*) led to better stability against necking. Thus, CMTs appear to be more stable against necking when the density of the ECM is increased and

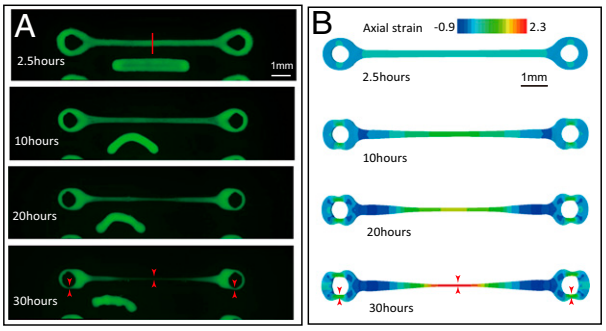

Fig. 2. Experimental observations (*A*) and 3D finite element simulations (*B*) of necking and failure of loop-ended dog bone-shaped (tissue self-assembled in recesses consisting of two toroidal shapes surrounding circular pegs connected by a central trough) microtissues. The inner and outer radii of the tori are 400 μm and 1.2 mm, respectively; the distance between the centers of the tori is 9 mm; and the width of the connecting rod is 800 μm. Red arrowheads indicate the locations of necking and failure. (*B*) Failure simulated using a 3D finite element model (failure occurs near the midpoint of the connecting rod). Contours of axial stretch are also given in the figure.

when the stiffness of the supporting cantilevers is decreased. In addition, Hansen et al. demonstrated that inhibiting ECM degradation was necessary to avoid failure in CMTs (15). These results confirm that cardiac tissues require high ECM densities to be stable over weeks.

Stability of Loop-Ended Dog-Bone Fibroblast and Hepatocyte Tissues. To study the morphological evolution and stability of constrained fibroblast tissues, we produced loop-ended dog bone-shaped microtissues from normal human fibroblasts (NHFs), using the self-assembly technique (without preformed ECM) described previously (3). Briefly, we cast nonadhesive hydrogel micromolds consisting of 2% (wt/vol) agarose in phosphate-buffered saline from PDMS micromold negatives. A suspension of NHFs fluorescently labeled with CellTracker Green 5-chloromethylfluorescein diacetate was then added to the inner chamber of each micromold. Over the next 20 min, the NHFs would settle into the recesses of the micromold and begin to self-assemble into microtissues consisting of two toroids connected by a rod. These loop-ended dog-bone microtissues were constrained at each end by micromold pegs rising through the lumen of each toroid. Upon self-assembly, the microtissue would compact as the individual NHFs adhered to one another. This, in turn, generated tension within the microtissue, manifested by thinning and elongation in the rod portion of the tissue. This thinning would eventually lead to necking and failure, at which point the resulting free ends of the rod would immediately contract to either toroid to relax tension within the tissue. Fig. 2*A* and *SI Appendix*, Fig. 12*A*, *Upper* and *Lower* depict the morphologies of microtissues which thinned near the center of the rod, at one side of the rod, and at two points along the rod, respectively.

SI Appendix, Fig. 11 depicts the evolution of the cross-sectional area near the center of the dog-bone microtissue. We find that the width decreases rapidly at all positions along the rod portion of the microtissue during the initial few hours after seeding. During the narrowing phase the majority of cells in the constrained connecting rod elongated dramatically to lengths over 30 times their starting diameters. In addition, after failure of the connecting rod, the resulting toroid microtissues would tighten around the constraining posts and thin, to the extent that they would often fail again at a single point, resulting in a curved, noncontiguous rod (*SI Appendix*, Fig. 12*C*). Altogether our results provide a detailed description of the morphological changes associated with the generation and relaxation of tension within a constrained microtissue. Elongation and failure of the microtissue were not observed in self-assembling unconstrained rods of similar size. The above experiments were repeated with rat hepatocyte (H35) cells which are much less contractile than NHFs. While cell–cell adhesions still drove the formation of dog-bone tissues, the H35 dog bones did not develop significant tension or fail and were found to be stable for at least a week (*SI Appendix*, Fig. 10).

Three-Dimensional Mechanosensing Model

To quantitatively analyze the complex morphological evolution described in the experiments above, we designed a three-element model that consists of two passive elastic elements to represent the elasticity of the series and parallel elements and an active contractile element, as shown in Fig. 3*A*. The stiffness of the tissue, in general, is expected to have components that act in series and in parallel to the active element. The series component, (E_C), which accounts for the stiffness of the actin filaments on which the myosin motors move and the stiffness of the cell–cell contacts, is added in series with the active element (representing the contractility of the tissue). The sum of the stiffnesses of the ECM and some passive contributions of the cell that act in parallel with the active element is denoted by E_P. With position vectors to a material point in the initial and current configurations given by $\mathbf{X}$ (*SI Appendix*, section 6) and $\mathbf{x}=\mathbf{x}(\mathbf{X},t)$, respectively, the total deformation gradient tensor is expressed as $\mathbf{F}=\nabla\mathbf{x}$, where $\nabla=\partial/\partial\mathbf{X}$. Since the parallel element deforms in parallel with the cells, their deformation gradients are the same. $\mathbf{F}=\mathbf{F}_P=\mathbf{F}_C\mathbf{F}_A$, where the subscripts P, A, and C are used to denote the contributions from the parallel passive elasticity, actomyosin activity, and the series passive elasticity, respectively. Note that here the deformation gradient of the cells is multiplicatively decomposed into active ($\mathbf{F}_A$) and passive components ($\mathbf{F}_C$).

To relate the stress at any material point to deformation, we have to consider constitutive laws for each of the mechanical components. The total stress at a material point is the sum of the passive stress from the series and parallel components, $\sigma=\boldsymbol{\sigma}_C(\mathbf{F}_C)+\boldsymbol{\sigma}_P(\mathbf{F}_P)$. Note that since the contractile element and the passive tissue element transmit the same forces (Fig. 3*A*), the active stress $\boldsymbol{\sigma}_A$ experienced by the actomyosin system is the same as the passive stress in the series component of tissue, $\boldsymbol{\sigma}_C$. For the passive strain-hardening response of the series and parallel elements, we use neo-Hookean hyperelastic stress–strain relations as described in *SI Appendix*, section 2.

Recent experiments on fibroblasts (12) subject to uniaxial loading have shown that their active stress vs. strain-rate response obeys the classic Hill relation (16) (*SI Appendix*, Eq. 1) at large stresses, while a deviation is observed at small applied stresses. According to the Hill relation (which applies to muscle-like sarcomere

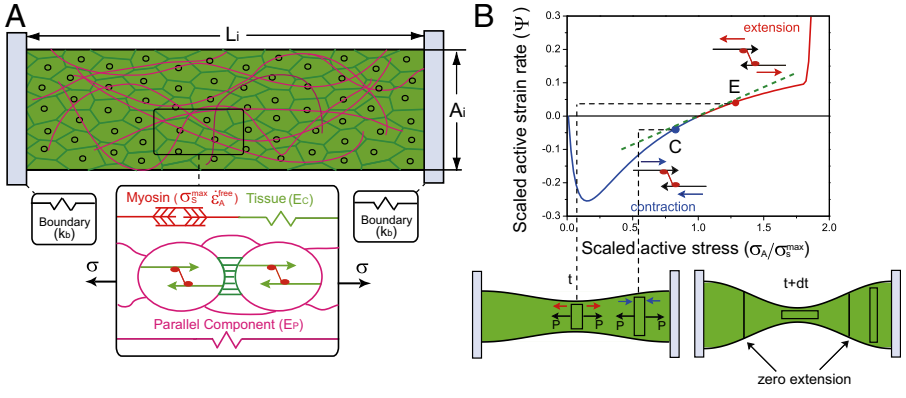

Fig. 3. (*A*) Three-dimensional mechanosensing model: (*Upper*) schematic of the constrained tissue (green) and the ECM (magenta) and (*Lower*) three-element model for the active tissue, where tissue stiffness (green), including cell stiffness (light green) and cell–cell contact stiffness (dark green), are modeled using a hyperelastic constitutive relation (with tangent stiffness E_C) in series with the an active contractile element (red) that obeys a Hill-like stress vs. strain-rate relation. These components act in parallel with the ECM, whose tangent modulus is denoted by E_P (pink). Elastic boundaries are modeled as springs (black) with spring constant k_b. (*B*) The modified Hill force–velocity model for contraction of nonmuscle cells in contractile tissues (16). Black lines represent actin bundles and red lines with heads denote myosin motors. Blue and red arrows indicate stress fiber contraction and extension, respectively. The curve shows the variation of the normalized contraction rate Ψ as a function of normalized stress σ_A/σ_S^{max} for active tissues. The initial increase in the magnitude of stress is due to recruitment of actin filaments to form stress fibers; once these fibers are formed (as shown schematically by the oriented network on the top), the stress vs. strain-rate relation resembles that of a sarcomere. The physical origin of the necking instability in contractile tissues is shown schematically on the bottom. When a small perturbation is applied to the shape, such that the cross-sectional area of the point E (or C) is smaller (or greater) than the unperturbed area, increase (or decrease) in active stress relative to the stall stress leads to greater stretching (or contraction) of the tissue. This in turn leads to a further decrease (or increase) in the cross-sectional area and necking of the tissue. The green dashed line denotes the slope of the strain rate vs. stretch curve at the stall point (*K*).

structures) the contraction rate is largest in the absence of any applied stress, monotonically decreases with increasing tensile stress, and eventually vanishes when the applied stress equals the stall stress (*SI Appendix*, Fig. 1). However, for nonmuscle cells considered in this work, the density of stress fibers depends on the level of applied mechanical stresses due to the dependence of the biochemistry of actin polymerization and myosin phosphorylation on mechanical stresses (17–19); at low stress levels, the density of stress fibers and (hence the contractile strain) increases with increasing stress, eventually saturating at large enough stress levels. This is clearly illustrated by experiments on spreading of nonmuscle cells on deformable substrates—the forces the cells exert on the substrate through their contractile machinery initially increase as the stiffness of the substrate is increased, saturating on substrates of very large stiffness (11, 12). As we show in *SI Appendix*, section 1.2, when the coupling between biochemistry and mechanical stresses is considered, we obtain a curve that resembles the Hill curve with a monotonic decrease at large stresses close to the stall stress, but a non-monotonic relation at small stresses (Fig. 3*B*). It has also been seen that stress-fibers only form in nonmuscle cells in the presence of anisotropic stresses – for example, cells in collagen gels develop structural anisotropy and a high density of fibers under uniaxial loading, whereas isotropic stress fields do not lead to dense aligned fibers (20). Therefore, in our 3D large-deformation analysis, we assume that the active deformation rate depends only on the active deviatoric stress, but not on the pressure;

$$\frac{\mathbf{D}_A}{\dot{\epsilon}_A^{max}} = \frac{3}{2}\frac{\mathbf{S}_A}{\sigma_A}\Psi\left(\frac{\sigma_A}{\sigma_S^{max}}\right), \qquad [1]$$

where σ_S^{max} and $\dot{\epsilon}_A^{max}$ are the maximum values of the stall stress and contractile strain rate, respectively, and $\sigma_A = \sqrt{\frac{3}{2}\mathbf{tr}(\mathbf{S}_A\mathbf{S}_A)}$ is the equivalent active deviatoric stress in which $\mathbf{S}_A = \boldsymbol{\sigma}_A - \frac{1}{3}\mathbf{tr}(\boldsymbol{\sigma}_A)$. The function $\Psi\left(\frac{\sigma_A}{\sigma_S^{max}}\right)$ is plotted in Fig. 3*B*. Note also that the above equation (Eq. **1**) ensures that deformation due to active stresses are volume conserving. While more complex relations (that include compressibility effects) for active strain-rate response can be used (21), as we show in *SI Appendix*, section 1.2, the main features of necking and failure are captured with the simple form that we use here. Using the conditions for mechanical equilibrium and Eq. **1**, we have developed a finite element method to model the 3D morphological evolution of the tissue. The key features of the necking instabilities observed in our experiments can be understood quantitatively using the linear stability analysis that we consider next.

Stability of Constrained Microtissues: Linear Analysis and Failure Maps

To study the stability of the tissue due to spatial perturbations in shape or contractility, we first consider the case of the tissue of initial uniform cross-sectional area A_i suspended between flexible posts of stiffness k_b and initially separated by distance L_i, shown in Fig. 3*A*. When the tissue (assumed to be incompressible) contracts and equilibrates, the cross-sectional area in the deformed configuration can be related to the local stretch $\bar{\lambda}$ by $\overline{A} = A_i/\bar{\lambda}$ (the overline symbol is used to denote quantities in equilibrium). As we show in *SI Appendix*, section 2.4, equilibrium stretch and tension can be solved using the following equations obtained from the constitutive equations and the conditions for force balance in the tissue and at the boundaries:

$$\frac{\overline{P}}{A_i}\bar{\lambda} = \sigma_S^{max} + \sigma_P(\bar{\lambda}), \quad \text{and} \quad \overline{P} + k_b L_i\frac{(\bar{\lambda}-1)}{2} = 0, \qquad [2]$$

where $\sigma_P(\bar{\lambda})$ is the uniaxial constitutive relations for the parallel element, and $\overline{P}$ is the force exerted by the tissue and the ECM on a post. If the initial area of cross-section is a constant, as we show in *SI Appendix*, section 2.4, the steady-state stress that develops in the tissue is approximately given by

$$\overline{\sigma} = \frac{\sigma_S^{max}}{1 + \frac{2E_P^0 A_i}{k_b L_i}}, \qquad [3]$$

where E_P^0 is the tangent parallel stiffness at zero strain. Note that this stress increases with increasing stiffness of the posts (k_b) and decreasing parallel stiffness/ECM density (E_P^0). The maximum stress that is achieved in the limit of infinitely stiff posts and vanishing parallel stiffness is the characteristic stall stress of the tissue, σ_S^{max}.

Next, as in the case of necking analysis for passive materials (22), we apply an elastic perturbation to the tissue such that the cross-sectional area is altered by a small amount $\delta A(z,t)$ from the equilibrium area (Fig. 4*A*) and study the conditions under which these small perturbations can grow in an unstable manner leading to necking. For a tissue whose overall elastic response is incompressible, the perturbation in the area is accompanied by variations in stretch, such that $\delta\dot{\lambda}(z,t)/\bar{\lambda} = -\delta\dot{A}(z,t)/\overline{A}$. By using the hyperelastic constitutive laws for the parallel element and Eq. **1** and applying the boundary conditions at the posts (*SI Appendix*, section 2), we find that the perturbation evolves according to the equation

$$\frac{\dot{\delta\lambda}(z,t)}{\delta\lambda(z,t)} = -\overline{E_C}K\dot{\epsilon}_A^{max}\frac{\overline{E_P} - \overline{\sigma}}{\overline{E_C} + \overline{E_P} - \overline{\sigma}}, \qquad [4]$$

where $K = d\Psi/d\sigma_A$ is the slope of the contractile strain vs. stress curve (the green dashed line in Fig. 3*B*) and $\overline{E_C}$ and $\overline{E_P}$ are the tangent series and parallel stiffnesses in equilibrium, respectively.

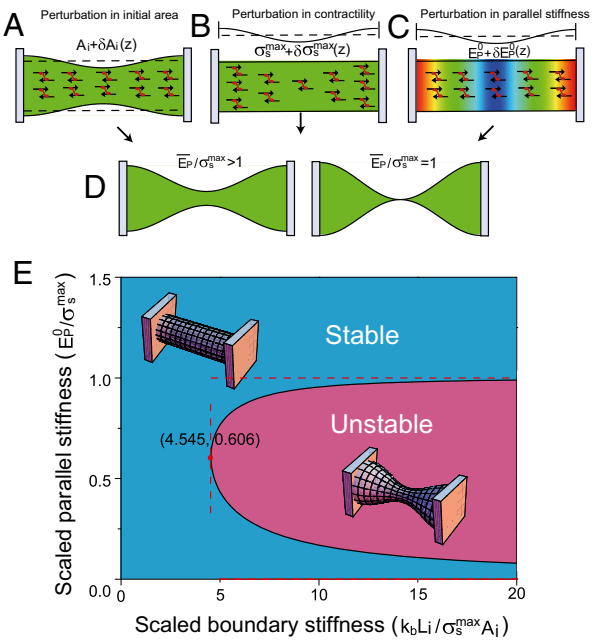

Fig. 4. Schematics of perturbations in the initial cross-sectional area, $A_i + \delta A_i(z)$ (*A*); contractility, $\sigma_S^{max} + \delta\sigma_S^{max}(z)$ (*B*); and ECM density/parallel stiffness, $E_P^0 + \delta E_P^0(z)$ (*C*) along the tissue. Colors in *C* (blue to red) represent variation in ECM density/parallel stiffness (low to high). (*D*) The morphology of the tissue is stable when $\overline{E_P}/\overline{\sigma} > 1$ and thins in an unstable manner, indicating the onset of necking, when $\overline{E_P}/\overline{\sigma} \to 1$. (*E*) Stability phase diagram plotted as a function of the scaled boundary stiffness $k_b L_i/\sigma_S^{max} A_i$ and the scaled parallel stiffness E_P^0/σ_S^{max}. Light blue and magenta represent stable and unstable regions, where the perturbations in *A*–*C* grow in an unstable manner as the phase boundary is approached.

For the tissue to be stable, the right-hand side of the above equation should be negative. The instability using the two-element model without a series component can be directly derived from Eq. **4** as $\overline{E_c} \to \infty$; the tissue is stable as $K\dot{\epsilon}_A^{max}(\overline{E_P} - \overline{\sigma}) > 0$, so the series passive components are not essential to obtain the instability. Using the expression for the steady-state stress in the tissue in *SI Appendix*, Eq. **17**, we have plotted a phase diagram that shows the regime of stability of the tissue as a function of two parameters, the scaled tangent parallel stiffness, E_P^0/σ_S^{max}, and the scaled stiffness of the posts, $k_b A_i/L_i\sigma_S^{max}$, in Fig. 4*E*. We find that the tissue is unstable when the scaled parallel and boundary stiffnesses are small and large, respectively. In particular, when the tissue is fully constrained, the tissue is only stable if the tangent parallel stiffness is larger than the stall stress, $E_P^0 > \sigma_S^{max}$. This suggests that in the absence of any parallel component, the active response of the constrained tissue renders the tissue unstable.

The physical origin of the instability of the tissue constrained by rigid posts can be qualitatively understood from Fig. 3*B*—here we consider the evolution of two regions, one whose area of cross-section is larger than the equilibrium value and the other whose area is smaller. Since the stress in the former (latter) case is smaller (larger) than the stall stress, we can see that the tissue contracts (stretches) in the former (latter) case. This in turn leads to further compression (stretching) in the regions whose perturbed area is larger (smaller) than the steady-state value, thus leading to the growth of the instability. The key physical feature that leads to the instability is the positive slope of the Hill curve (K) at the isometric point. When the ECM density is sufficiently large, the elastic response of the ECM counteracts the effects of the active response and is able to stabilize the tissue against necking. These results from the linear stability analysis qualitatively explain why the fibroblast tissues with no ECM fail much more easily by necking compared with the cardiac tissue constructs with large densities of ECM. Furthermore, the evolution of the perturbation depends on the steady-state stress, $\overline{\sigma}$, which in turn depends on the stiffness of the posts. Decreasing the stiffness of the posts also leads to a decrease in stress and renders the tissue more stable, in agreement with our experiments.

While we have considered elastic perturbations to a uniformly contracted state, inhomogeneities in the seeding of the tissue can lead to variations in the initial cross-sectional area of the tissue (A_i), the number density of the cells (and hence the maximum stall stress, σ_S^{max}), and the density (and hence the stiffness, E_P^0) of the ECM. These variations in turn will lead to variations in cross-sections and stretches along the length of the tissue in equilibrium (Fig. 4*D*). Using the prefix δ to denote variations in the chemomechanical material parameters, we show in *SI Appendix* that the variation in stretches along the tissue can be written as

$$\frac{\delta\bar{\lambda}(z)}{\bar{\lambda}} = \frac{-1}{\overline{E_P} - \overline{\sigma}}\left[\overline{\sigma}\frac{\delta A_i(z)}{A_i} + \delta\sigma_S^{max}(z) + \overline{\sigma_P}\frac{\delta E_P^0(z)}{E_P^0}\right]. \qquad [5]$$

The above result shows that for a given density of ECM, the variations in stretches increase with increasing contractility and hence $\overline{\sigma}$ or σ_S^{max}; the variations diverge when $\overline{\sigma} \to \overline{E_P}$, indicating the onset of necking (Fig. 4*D*). No physically admissible solutions can be found when $\overline{\sigma} > \overline{E_P}$ (*SI Appendix*, sections 2.2 and 2.3). Note that the conditions for stability found for the variations in the initial material parameters are the same as the conditions found for the elastic perturbations in shape, illustrating the general applicability of these criteria.

Three-Dimensional Finite Element Simulations of Tissue Morphology Evolution and Failure

To model the evolution of the tissue for large deformations, we implemented the hyperelastic constitutive equations and Eq. **1** in a user material model in the finite element package ABAQUS (23). The details of the user material implementation are given in *SI Appendix*. Simulations of the evolution of the morphology of the fibroblast tissue are shown in Fig. 2*B* and *SI Appendix*, Fig. 12*B*. Here we start by applying perturbations in shape (amplitude 5% of the thickness) to an otherwise symmetric dog-bone shape at different positions along the length of the connecting rod. Although the magnitudes of the initial perturbations are too small to be seen early on (Fig. 2*B*, *Upper*), the perturbations grow in amplitude with time. Our simulations are able to faithfully reproduce all aspects of the evolution of the perturbations including thinning and extension at points where the perturbations are applied and thickening at regions close to the peg. When the perturbations are applied at two points (*SI Appendix*, Fig. 12*B*, *Lower*), one close to the end and the other near the middle, thinning is observed at both points initially, although the point at the center eventually thins much more rapidly during the later stages of evolution, in agreement with observations. By fitting the computed cross-sectional area along the connecting rod with experimental measurements (*SI Appendix*, Fig. 11), we are able to quantify all of the parameters in our constitutive model. We find that the initial series stiffness, $E_C^0 = 5\sigma_S^{max}$, the initial parallel stiffness, $E_C^0 = 0.08\sigma_S^{max}$, and the maximum rate of active contraction, $\dot{\epsilon}_A^{max} = 4.25 \times 10^{-4}/s$. The rate of active contraction we have deduced from the simulations of tissue morphology is close to the value $8.25 \times 10^{-4}/s$ measured for single fibroblasts held between flexible plates (12), lending strong support to our analysis. Since the parallel stiffness in these tissues is only a small fraction of the stall stress, the failure of the tissue observed in the experiments is consistent with the phase diagram in Fig. 4*E*. We observe greater rates of contractility in tissues treated with TGF-β, confirming that TGF-β enhances actomyosin activity. The failure of toroidal ends after the failure of the central band is discussed in *SI Appendix*, section 9.

In the case of the CMTs, we carried out simulations to model the evolution of the tissue from day 0 to day 7 and monitored both the force exerted by the tissue on the cantilevers and the shape of the tissue (Fig. 1 *C* and *D*). On day 3, we applied an isotropic contractile strain of 1% to mimic the formation of cell–cell contacts and the compaction process. By fitting six sets of measured tissue force and area vs. time curves (Fig. 1 *C* and *D*) to our simulations (using the least squares method described in *SI Appendix*), we determined the following material parameters: series stiffness, $E_C^0 = 10$ kPa; maximum stall stress, $\sigma_S^{max} = 0.5$ kPa; maximum rate of active contraction, $\dot{\epsilon}_A^{max} = 1.65 \times 10^{-4}/s$; and the initial parallel stiffness, $E_P^0 = 0.125$ kPa for 1.0 mg/mL collagen and $E_P^0 = 0.175$ kPa for 2.5 mg/mL collagen, respectively. The initial stiffness of the ECM increases with deformation following the neo-Hookean constitutive law. Our simulations clearly explain why the tissue is much more stable to necking (Fig. 1 *E*–*G*) when the ECM density is large and the cantilevers flexible.

We also find that the parameters we have obtained here are consistent with properties of cardiac tissues reported in the literature. There are 58% cardiomyocytes and 42% nonmyocytes (mostly fibroblasts) in our CMTs (6). The Young's modulus of fibroblast tissue has been reported to be in the range of 4 to 5 kPa (24) and the Young's modulus of myocardium is around 10–20 kPa (25). The value we obtained for series stiffness, $E_C = 10$ kPa, lies between the stiffness of cardiomyocytes and fibroblasts. Also, the stiffness of heart muscle has been reported to be 10–20 kPa at the beginning of diastole (26), consistent with the values we obtained using our fitting procedure. The elastic modulus of fibroblast microtissues has been reported as 20–40 kPa, depending on the chemical treatment (27). The mechanical properties of collagen–fibrin cogels (0–2.1 mg/mL collagen and 0–3.0 mg/mL fibrin) have been measured experimentally and fitted using a nonlinear stress–strain relation (28). Pure collagen (2.1 mg/mL) possesses a much higher stiffness and a larger degree of nonlinearity than pure fibrin (3.0 mg/mL), suggesting that the mechanical behavior of a collagen/fibrin ECM is dominated by the response of collagen. The Young's modulus at small strains has been reported to be 0.2 kPa for 2.1 mg/mL pure collagen; the values we obtain (0.125 kPa for 1.0 mg/mL collagen and 0.175 kPa for 2.5 mg/mL collagen) are therefore in this range.

Discussion and Future Work

In passive materials, necking is generally understood on the basis of the classic Considère instability (29), which provides a criterion for failure based on passive elastic response. According to this criterion, necks form in strain-softening materials under tension when regions of the material with reduced area (and hence larger stresses) rapidly elongate. This occurs if the material does not sufficiently strain harden to compensate for the increased stresses in narrowed regions. This model however cannot explain the necking observed in the active tissues that we consider here because (*i*) it is well established that the passive response of the cytoskeletal components of the cells as well as the tissues themselves is generally of a strain-hardening nature (30) and because (*ii*) this model does not account for the active response of the material. As we have shown here, necking can be observed even in active materials with a passive strain-hardening response. Models have also been developed to include the role of actomyosin activity using continuum and discrete approaches (21, 31–37), but none of these models account for the coupling between geometry, stress, and the actomyosin activity responsible for the dramatic evolution of morphology observed in constrained microtissues (Figs. 1 and 2). The predictions of our model are also consistent with the observations of necking and failure in constrained reconstituted actomyosin gels made using skeletal muscle myosin II-thick filaments, actin and α-actinin (38). Interestingly, unconstrained gels were found to be stable, indicating that the observed instability is caused by the mechanism proposed in this work.

Three-dimensional tissue constructs have served as in vitro models of tissue morphogenesis and wound healing, and, more recently, designs such as honeycombs and toroids have been proposed as strategies for drug delivery and in vivo implantation (4). In natural tissues, actomyosin activity is significantly influenced by whether the cells see a homotypic or heterotypic environment (39). We have recently shown that the self-assembly forces exerted by cells in the mixed heterotypic cell environment are significantly greater than the forces in their respective homotypic environments. Extension of the work described here to study the stability of tissue constructs with multiple cell types of different stiffness would be of fundamental relevance to tissue engineering as well as developmental biology because natural tissues are not composed of a single cell type. They are a mix of cell types and there are few, if any, means to quantify these interactions in 3D. In natural tissues, cells also assemble a dense meshwork of ECM proteins, including collagen, fibronectin, tenascin, and other proteins. Understanding how forces arising from contractility influence the formation of these proteins and how increased stiffening of the tissue due to these proteins regulates contractility can provide insights into the mechanisms of branching of blood vessels and bronchial tubes, shaping of organs, and embryogenesis (40, 41).

ACKNOWLEDGMENTS. We thank Dr. Ananth Chopra for help with protein immunoblot experiments. This work is supported by US National Science Foundation Grant CMMI-1312392.

1. Hotulainen P, Lappalainen P (2006) Stress fibers are generated by two distinct actin assembly mechanisms in motile cells. *J Cell Biol* 173(3):383–394.
2. Pollard TD, Wu JQ (2010) Understanding cytokinesis: Lessons from fission yeast. *Nat Rev Mol Cell Biol* 11(2):149–155.
3. Dean DM, Rago AP, Morgan JR (2009) Fibroblast elongation and dendritic extensions in constrained versus unconstrained microtissues. *Cell Motil Cytoskeleton* 66(3): 129–141.
4. Dean DM, Napolitano AP, Youssef J, Morgan JR (2007) Rods, tori, and honeycombs: The directed self-assembly of microtissues with prescribed microscale geometries. *FASEB J* 21(14):4005–4012.
5. Legant WR, et al. (2009) Microfabricated tissue gauges to measure and manipulate forces from 3D microtissues. *Proc Natl Acad Sci USA* 106(25):10097–10102.
6. Boudou T, et al. (2012) A microfabricated platform to measure and manipulate the mechanics of engineered cardiac microtissues. *Tissue Eng Part A* 18(9-10):910–919.
7. Thomas S, et al. (2011) Src and caveolin-1 reciprocally regulate metastasis via a common downstream signaling pathway in bladder cancer. *Cancer Res* 71(3):832–841.
8. Castella LF, Buscemi L, Godbout C, Meister JJ, Hinz B (2010) A new lock-step mechanism of matrix remodelling based on subcellular contractile events. *J Cell Sci* 123(Pt 10): 1751–1760.
9. Discher DE, Janmey P, Wang YL (2005) Tissue cells feel and respond to the stiffness of their substrate. *Science* 310(5751):1139–1143.
10. Saez A, Buguin A, Silberzan P, Ladoux B (2005) Is the mechanical activity of epithelial cells controlled by deformations or forces? *Biophys J* 89(6):L52–L54.
11. Ghibaudo M, et al. (2008) Traction forces and rigidity sensing regulate cell functions. *Soft Matter* 4(9):1836–1843.
12. Mitrossilis D, et al. (2009) Single-cell response to stiffness exhibits muscle-like behavior. *Proc Natl Acad Sci USA* 106(43):18243–18248.
13. Steinberg MS (1962) Mechanism of tissue reconstruction by dissociated cells. II. Time-course of events. *Science* 137(3532):762–763.
14. Foty RA, Steinberg MS (2005) The differential adhesion hypothesis: A direct evaluation. *Dev Biol* 278(1):255–263.
15. Hansen A, et al. (2010) Development of a drug screening platform based on engineered heart tissue. *Circ Res* 107(1):35–44.
16. Hill AV (1938) The heat of shortening and the dynamic constants of muscle. *Proc R Soc Lond B Biol Sci* 126(843):136–195.
17. Burridge K, Chrzanowska-Wodnicka M (1996) Focal adhesions, contractility, and signaling. *Annu Rev Cell Dev Biol* 12:463–518.
18. Mochitate K, Pawelek P, Grinnell F (1991) Stress relaxation of contracted collagen gels: Disruption of actin filament bundles, release of cell surface fibronectin, and down-regulation of DNA and protein synthesis. *Exp Cell Res* 193(1):198–207.
19. Grinnell F (1994) Fibroblasts, myofibroblasts, and wound contraction. *J Cell Biol* 124(4):401–404.
20. Thomopoulos S, Fomovsky GM, Holmes JW (2005) The development of structural and mechanical anisotropy in fibroblast populated collagen gels. *J Biomech Eng* 127(5): 742–750.
21. Deshpande VS, McMeeking RM, Evans AG (2006) A bio-chemo-mechanical model for cell contractility. *Proc Natl Acad Sci USA* 103(38):14015–14020.
22. Hutchinson JW, Neale KW (1977) Influence of strain-rate sensitivity on necking under uniaxial tension. *Acta Metall* 25(8):839–846.
23. ABAQUS Manual (2010) (Dassault Systemes, Providence, RI), Version 6.10.
24. Bushell GR, et al. (1999) Imaging and force-distance analysis of human fibroblasts in vitro by atomic force microscopy. *Cytometry* 36(3):254–264.
25. Berry MF, et al. (2006) Mesenchymal stem cell injection after myocardial infarction improves myocardial compliance. *Am J Physiol Heart Circ Physiol* 290(6):H2196–H2203.
26. Chen QZ, et al. (2008) Characterisation of a soft elastomer poly(glycerol sebacate) designed to match the mechanical properties of myocardial tissue. *Biomaterials* 29(1): 47–57.
27. Zhao RG, Boudou T, Wang WG, Chen CS, Reich DH (2013) Decoupling cell and matrix mechanics in engineered microtissues using magnetically actuated microcantilevers. *Adv Mater* 25(12):1699–1705.
28. Lai VK, Lake SP, Frey CR, Tranquillo RT, Barocas VH (2012) Mechanical behavior of collagen-fibrin co-gels reflects transition from series to parallel interactions with increasing collagen content. *J Biomech Eng* 134(1):011004.
29. Considère A (1885) *Ann Ponts Chaussees* 9:574–775.
30. Storm C, Pastore JJ, MacKintosh FC, Lubensky TC, Janmey PA (2005) Nonlinear elasticity in biological gels. *Nature* 435(7039):191–194.
31. Schwarz US, Erdmann T, Bischofs IB (2006) Focal adhesions as mechanosensors: The two-spring model. *Biosystems* 83(2-3):225–232.
32. Besser A, Schwarz US (2007) Coupling biochemistry and mechanics in cell adhesion: A model for inhomogeneous stress fiber contraction. *N J Phys* 9(11):425.
33. Zemel A, Rehfeldt F, Brown AEX, Discher DE, Safran SA (2010) Optimal matrix rigidity for stress fiber polarization in stem cells. *Nat Phys* 6(6):468–473.
34. Guthardt Torres P, Bischofs IB, Schwarz US (2012) Contractile network models for adherent cells. *Phys Rev E Stat Nonlin Soft Matter Phys* 85(1):011913.
35. Köpf MH, Pismen LM (2013) A continuum model of epithelial spreading. *Soft Matter* 9(14):3727–3734.
36. Mertz AF, et al. (2013) Cadherin-based intercellular adhesions organize epithelial cell-matrix traction forces. *Proc Natl Acad Sci USA* 110(3):842–847.
37. Banerjee S, Marchetti MC (2011) Instabilities and oscillations in isotropic active gels. *Soft Matter* 7(2):463–473.
38. Bendix PM, et al. (2008) A quantitative analysis of contractility in active cytoskeletal protein networks. *Biophys J* 94(8):3126–3136.
39. Youssef J, Chen P, Shenoy VB, Morgan JR (2012) Mechanotransduction is enhanced by the synergistic action of heterotypic cell interactions and TGF-β1. *FASEB J* 26(6): 2522–2530.
40. Taber LA (2000) Pattern formation in a nonlinear membrane model for epithelial morphogenesis. *Acta Biotheor* 48(1):47–63.
41. Taber LA, Zahalak GI (2001) Theoretical model for myocardial trabeculation. *Dev Dyn* 220(3):226–237.

Supplementary information appendix for "Necking and failure of constrained 3D microtissues induced by cellular tension"

Hailong Wang[a], Alexander A. Svoronos[b], Thomas Boudou[c], Mahmut Selman Sakar[d], Jacquelyn Youssef Schell[b], Jeffrey R. Morgan[b], Christopher S. Chen[c] and Vivek B. Shenoy[a,*]

[a]Department of Materials Science and Engineering and [c]Department of Bioengineering, University of Pennsylvania, Philadelphia, PA 19104; [b]Department of Molecular Pharmacology, Physiology and Biotechnology, Center for Biomedical Engineering, Brown University, Providence, RI 02912; [d]Institute of Robotics and Intelligent Systems, ETH Zurich, Zurich, CH 8092, Switzerland *To whom correspondence should be addressed. Email: vshenoy@seas.upenn.edu

1 Active constitutive law for contractile tissues

In this section we derive the active constitutive law given by Eq. (1) of the main text. Our derivation involves three steps:

1. We start with the classic Hill-relation [1], which provides a relation between the active contraction rate and the applied stress, and consider the scenario (that applies to non-muscle cells) where the density of stress fibers (and thus the maximum contraction rate and the stall stress) are functions of the applied stress.

2. Using the results from 1) and the fact that the time scales for stress dependent mechanisms for stress fiber formation are faster than the time scales for contractile dynamics (characterized by the active contraction rate) [2–4], we derive a modified version of the Hill's relation between active contraction rate and applied stress that accounts for stress dependence of fiber formation.

3. Based on the facts that only anisotropic stresses lead to the formation of fibers [5] and the overall mechanical response of the tissue is nearly incompressible, we generalize the 1D result obtained in the previous step to obtain the 3D version of the Hill-relation given by Eq. (1) of the main text.

1.1 Hill's Stress-strain rate relation

It has been recently demonstrated that single cells obey the Hill-relation [6] and contract with smaller speeds when subject to increasing force. For a tissue made up of these non-muscle cells, we

can generalize the force-velocity relation to a stress-strain rate relation to obtain:

$$\begin{aligned} \frac{\dot{\epsilon}_A}{\dot{\epsilon}_A^{free}} &= r\left(1 - \frac{r+1}{\frac{\sigma_A}{\sigma_S} + r}\right), \qquad 0 \leqslant \frac{\sigma_A}{\sigma_S} < \alpha \\ \frac{\dot{\epsilon}_A}{\dot{\epsilon}_A^{free}} &= k\left(\frac{\sigma_A}{\sigma_S} - \alpha\right) + \beta, \qquad \frac{\sigma_A}{\sigma_S} \geqslant \alpha \end{aligned} \tag{1}$$

where σ_S and $\dot{\epsilon}_A^{free}$ denote the stall stress and the contraction rate in the absence of applied stresses, respectively. The parameters β and α give a measure of the tensile yield strength of the fibers; when the applied stress satisfies the condition, $\sigma_A > \alpha\sigma_S$, the contractile bridge yields (i.e. flows without further increase in stress). In this regime the slope of the stress-strain rate curve is large (we take $k = 100$). Hill's experiments suggest that $\alpha \approx 1.8$ and $\beta \approx 0.1$. The parameter r is related to α and β through $\beta = r[1 - (r+1)/(\alpha + r)]$.

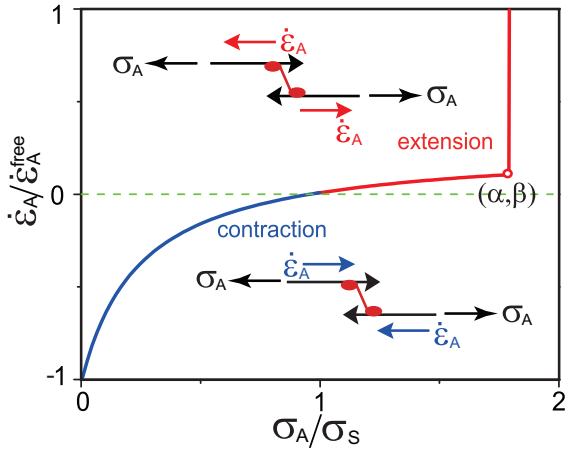

Figure 1: Stress-strain rate relation based on Hill-law. Black lines represent actin bundles and the red lines with heads denote myosin motors. Blue and red arrows indicate contraction and extension of the stress fibres, respectively.

1.2 Tension-dependent myosin recruitment and saturation

Both stall stress, σ_S, and contraction rate, $\dot{\epsilon}_A^{free}$, increase with myosin recruitment and stress fiber formation as shown by recent experiments on the contractility of 3T3 fibroblasts [6]. For example, contracting fibroblasts can create tension to tear the surrounding gel. In floating gels, the fibroblasts lack stress fibers, and only 10% contraction is observed [7]. In distinct contrast, the stress fibers dramatically increase, and isometric tension is generated in anchored gels [8]. In anchored gels, once tension is released, the fibers start to disassemble after rapid contraction [8, 9]. When shear stress is applied to a localized site on the cell surface, an actin filament bundle can immediately develop adjacent to this site [10]. It has also been shown that the contractility of cells saturates at higher stress fiber concentrations. The traction forces exerted by 3T3 fibroblasts on flexible substrates

or cantilevers can reach a saturation plateau at high rigidities [6, 11], indicating that biochemical recruitment of myosin saturates at high levels of mechanical stress.

Using σ_S^{max} and $\dot{\epsilon}_A^{max}$ to denote the maximum stall stress and maximum contraction rate allowed by biochemistry (when the stress fibers are fully formed), respectively, we now derive expressions for the stall stress and rate of contraction at a given stress level, σ_A. For simplicity, we assume that the ratio of the current and maximum levels of stall stress and contraction rates scale in an identical manner with applied stress. Using the symbol η to denote this ratio, we then have

$$\eta = \frac{\sigma_S}{\sigma_S^{max}} = \frac{\dot{\epsilon}_A^{free}}{\dot{\epsilon}_A^{max}}. \tag{2}$$

To study the evolution of this parameter, we adapt the first order kinetic model proposed by Deshpande et al. [12]. We assume that the stress formation (dissociation) depends on the applied stress, σ_A, such that an increased stress level leads to an increase(decrease) in the formation (dissociation) of the fibers. Using k_f and k_d to denote rates of formation and dissociation of the fibers, we have

$$\begin{aligned} \dot{\eta} &= \frac{\sigma_A}{\sigma_S} k_f (1-\eta) - k_d \eta (1 - \frac{\sigma_A}{\sigma_S}), \quad 0 \leqslant \frac{\sigma_A}{\sigma_S^{max}} < 1 \\ \dot{\eta} &= k_f (1-\eta), \qquad\qquad\qquad\qquad \frac{\sigma_A}{\sigma_S^{max}} \geqslant 1 \end{aligned} \tag{3}$$

It has been shown that the time scales for polymerization-depolymerization of actin leading to stress-fiber formation are much faster than the time scales for cross-bridge dynamics [2–4]. Since the stall stress adapts to its steady-state value in this limit, we can set $\dot{\eta}$ in Eq. (3) to zero, yielding the relation

$$\begin{aligned} \eta &= \frac{1}{2\chi}[\sqrt{(1-\chi)^2 (\frac{\sigma_A}{\sigma_S^{max}})^2 + 4\chi \frac{\sigma_A}{\sigma_S^{max}}} - (1-\chi)\frac{\sigma_A}{\sigma_S^{max}}], \quad 0 \leqslant \frac{\sigma_A}{\sigma_A^{max}} < 1 \\ &= 1, \qquad\qquad\qquad\qquad\qquad\qquad\qquad\qquad\qquad \frac{\sigma_A}{\sigma_S^{max}} \geqslant 1 \end{aligned} \tag{4}$$

where the non-dimensional constant $\chi = k_d/k_f = 0.1$ [12]. We have also verified that the steady state approximation holds for tissues held between two flexible posts (Fig. 1 of the main text). By simulating the evolution of the activation level η and the normalized applied stress σ_A/σ_A^{max}, we found that the approximate formula in Eq. (4) provides an excellent description of the dependence of the stall stress on the applied stress (refer to Fig. 2). After substituting the equation for the stall stress from Eq. (4) in to the Hill law for cross-bridge dynamics, Eq. (1), the nondimensional active strain rate $\dot{\epsilon}_A/\dot{\epsilon}_A^{max}$ can be expressed in terms of the function $\Psi(\sigma_A/\sigma_S^{max})$ (plotted in Fig. 3B of the main text).

To extend the 1D model of stress fiber formulation to 3D, we first note that highly oriented stress fibers form only in the presence of anisotropic stresses; isotropic stresses do not give rise to a large density of fibers [5]. It has been shown that high degrees of fiber alignment are developed in fibroblast-populated collagen gels constrained uniaxially, and collagen gels remain isotropic under biaxial load [5]. Furthermore, if the tissue is incompressible, the rate of active deformation tensor should depend only on the active deviatoric stress, $\mathbf{S}_A = \boldsymbol{\sigma}_A - \frac{1}{3}\mathbf{tr}(\boldsymbol{\sigma}_A)$; we find that the expression

$$\frac{\mathbf{D}_A}{\dot{\epsilon}_A^{max}} = \frac{3}{2}\frac{\mathbf{S}_A}{\sigma_A}\Psi(\frac{\sigma_A}{\sigma_S^{max}}), \tag{5}$$

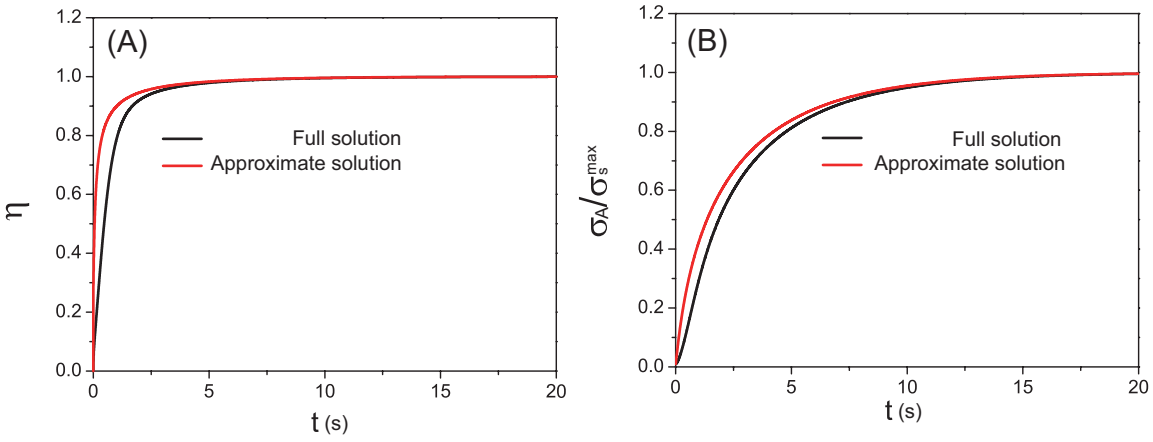

Figure 2: The time evolution of activation level η and normalized applied stress σ_A/σ_A^{max} using full and approximate solutions for a tissue held between two posts as shown in Fig. 1 of the main text. We estimate the material properties of cross-bridge dynamics and stress fiber formation from a previous study [12] and our fits to experiments on CMTs (refer to main text): $\sigma_S^{max} = 3.9$ kPa, $\dot{\epsilon}_A^{max} = 2.8 \times 10^{-4}$ s^{-1}, $k_f = 1.4 \times 10^{-2}$ s^{-1} and $k_d = 1.4 \times 10^{-3} s^{-1}$. The boundary stiffness and geometric size are obtained from Ref. [13]: $k_b = 0.2 - 0.45$ N/m, $L_i = 500$ μm, $A_i = 0.02$ mm^2.

where $\sigma_A = \sqrt{\frac{3}{2}\mathbf{tr}(\mathbf{S}_A\mathbf{S}_A)}$, the equivalent active stress, ensures that the active deformation rate is non-zero in the presence of anisotropy (simple pressure will not lead to stress fiber formation). Moreover, for the case of uniaxial deformation, where only one of the stress components are non-zero, the above expression reduces to the modified version of the Hill-expression.

2 Stability of the constrained tissue

In this section we provide a detailed derivation of the conditions for equilibrium of the tissue constrained between flexible posts and the criteria for the stability of the tissue. We first consider the case of the tissue with uniform cross-sectional area. In this case, all field variables depend only on the spatial coordinate, z, which is perpendicular to the cross-sectional area of the tissue and runs along the axis of the tissue (Fig. 4). Note that when the cross-sectional area is slightly perturbed, to linear order in the perturbations, shear stresses can be ignored [14,15]; therefore, only normal stresses are retained here. Furthermore, in equilibrium, the radial and hoop components of the stress vanish. Using λ_i and σ_i (with $i = A, C, P$) to denote the stretches and true (Cauchy) stresses, the constitutive laws (the hyperelastic constitutive law and Eq. (1) of the main text) can be written as

$$\sigma_C = \frac{E_C^0}{3}\left(\lambda_C^2 - \frac{1}{\lambda_C}\right), \quad \sigma_P = \frac{E_P^0}{3}\left(\lambda_P^2 - \frac{1}{\lambda_P}\right), \quad D_A = \frac{\dot{\lambda}_A}{\lambda_A} = \dot{\epsilon}_A^{max}\Psi\left(\frac{\sigma_A}{\sigma_S^{max}}\right), \tag{6}$$

where we have assumed that the series and parallel passive response follow the incompressible neo-hookean hyperelastic constitutive behavior with tangent stiffness E_i^0 $(i = C, P)$. The kinematics of

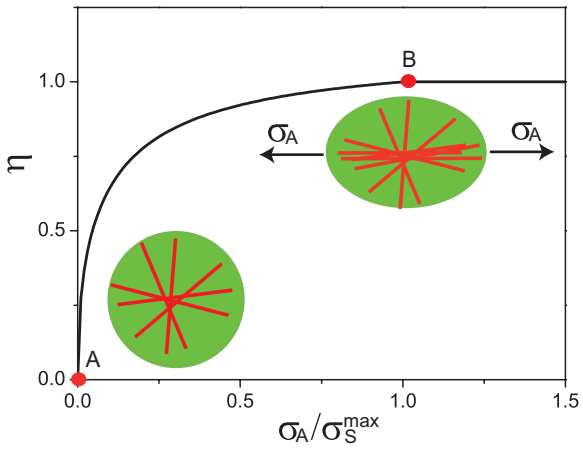

Figure 3: Activation level η vs normalized applied stress σ_A/σ_S^{max} for active tissues.

deformation of the 3-element model (Fig. 3A in the main text) require that

$$\lambda_C \lambda_A = \lambda_P = \lambda \quad \text{and} \quad \frac{\dot{\lambda}_A}{\lambda_A} + \frac{\dot{\lambda}_C}{\lambda_C} = \frac{\dot{\lambda}}{\lambda}, \tag{7}$$

where λ is the total stretch of the tissue. When the conditions of mechanical equilibrium are enforced for the 3-element model in the presence of constraining end-posts (refer to Fig. 3A in the main text), we get

$$\frac{P}{A_i}\lambda = \sigma_C + \sigma_P, \quad \text{and} \quad P = \frac{1}{2}k_b L_i \left(1 - \lambda\right), \tag{8}$$

where P is the force exerted by the tissue on the posts and A_i and L_i are the initial area of the cross-section and the length of the tissue, respectively (at the instant when the posts just start to move). Combining Eqs. (7) and (8) we get the equation

$$\frac{\dot{P}}{A_i}\lambda + \frac{P}{A_i}\dot{\lambda} = \left[\frac{\partial \sigma_C}{\partial \lambda_C}\lambda_C + \frac{\partial \sigma_P}{\partial \lambda}\lambda\right]\frac{\dot{\lambda}}{\lambda} - \frac{\partial \sigma_C}{\partial \lambda_C}\lambda_C \dot{\epsilon}_A^{max} \Psi\left(\frac{\sigma_A}{\sigma_S^{max}}\right) \tag{9}$$

for the time evolution of the stretch and force on the posts. For a tissue with uniform initial area of cross-section, as the tissue contracts, the force in the posts increases until the stress in the active element reaches the maximum allowed stall stress, at which point the contraction stops. In this equilibrium configuration, the stretch in the tissue and the force in the posts can be obtained by solving the equations

$$\begin{aligned} \overline{\sigma} &= \frac{\overline{P}}{A_i}\overline{\lambda} = \sigma_S^{max} + \frac{E_P^0}{3}\left(\overline{\lambda}^2 - \frac{1}{\overline{\lambda}}\right), \\ \overline{P} &= \frac{1}{2}k_b L_i (1 - \overline{\lambda}), \end{aligned} \tag{10}$$

where the overbars denote quantities in equilibrium and $\sigma_C = \sigma_S^{max}$ in equilibrium.

Next, we consider perturbations to the uniform shape and material parameters and assess the role of these perturbations on the morphology of the tissue in order to determine the stability of the tissue. In particular, we consider three cases:

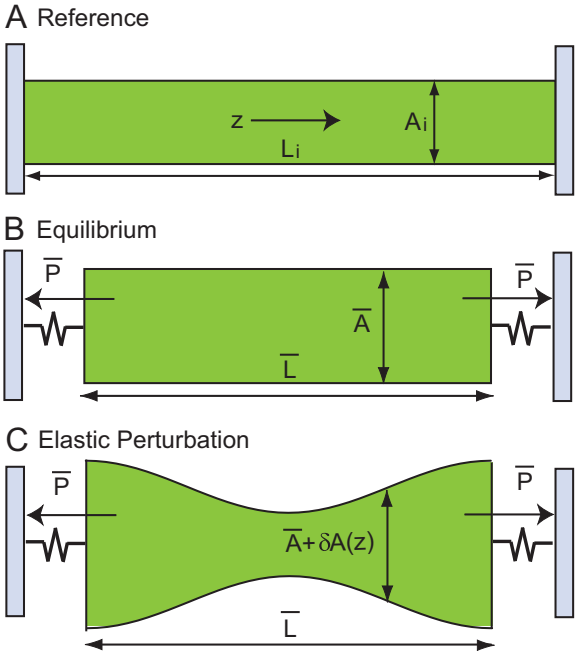

Figure 4: Schematics of the reference configuration(A), the equilibrium configuration (B) and the elastic perturbation (C) along the z axis of the constrained tissue.

1. We apply shape perturbations to the constrained uniform tissue in equilibrium and study how the perturbations grow with time.

2. In the analysis of equilibrium, we assumed that the initial area of cross-section was uniform. Below, consider the case where the initial area varies slightly along the axial direction and solve for the equilibrium configuration of the tissue.

3. We also assumed that the material parameters, in particular the maximum stall stress and the parallel stiffness, are constant across the tissue. Below we consider the case where these quantities can vary along the length of the tissue and determine the effect of these perturbations on the morphology of the tissue.

As we show below, in case 1, the applied perturbations in shape grow, and in cases 2 and 3, the perturbations diverge in an unstable manner when the tangent parallel stiffness is below the stress in equilibrium, $\overline{\sigma}$.

2.1 Stability of elastic perturbations

As noted in the main text, the perturbations we apply to the equilibrium shape are such that the net volume of the tissue is conserved. Writing $\lambda(z,t) = \overline{\lambda} + \delta\lambda(z,t)$, the change in area can be solved by invoking incompressiblity of the tissue,

$$\left(\overline{\lambda} + \delta\lambda(z,t)\right)\left(\overline{A} + \delta A(z,t)\right) = \overline{\lambda}\,\overline{A} = A_i, \tag{11}$$

from which, we obtain

$$\frac{\delta\lambda(z,t)}{\overline{\lambda}} = -\frac{\delta A(z,t)}{A_i}\overline{\lambda}. \tag{12}$$

Without loss of generality, we can choose the perturbation such that $\int_0^{L_i} \delta\lambda(z,t)dz = 0$. When this condition is used in Eq. (8), we find that there is no change in the force at the posts in the perturbed configuration, or $\delta P = 0$. Using the above relations in Eq. (9) and noting that $\Psi = 0$ in equilibrium, to linear order in perturbations, we obtain

$$\frac{\dot{\delta\lambda}(z,t)}{\delta\lambda(z,t)} = -\overline{E_C}K\dot{\epsilon}_A^{max}\frac{\overline{E_P} - \overline{\sigma}}{\overline{E_C} + \overline{E_P} - \overline{\sigma}} \tag{13}$$

where $E_i = d\sigma_i/d\epsilon_i$ ($i = C, P$ and $\epsilon_i = \log(\lambda_i)$ is the logarithmic strain) is the tangent stiffness and $K = d\Psi/d\sigma_A$. Since the tissue is modeled as a hyperelastic material, we have $\overline{E_C} > \overline{\sigma_C}$. Because $\overline{\sigma} = \overline{\sigma}_C + \overline{\sigma}_P$ and $\overline{\sigma}_P < 0$ (as $\overline{\lambda} < 0$), we also have $\overline{E_C} > \overline{\sigma}$. Therefore the denominator of the right-hand side of Eq. (13) is always positive. The stability of the tissue then depends on the sign of the numerator; the perturbations grow in an unstable manner if $\overline{E_P} < \overline{\sigma}$.

2.2 Perturbations in the initial shape

In the analysis above we assumed that the cross-sectional area of the tissue prior to contraction was uniform throughout the length of the tissue. Here we consider the consequences of variations in the initial shape, $A_i + \delta A_i(z)$, which can arise, for example, due to uneven seeding of the tissue. Without loss of generality, we assume that $\int_0^{L_i} \delta A_i(z)dz = 0$. The perturbation in initial shape will lead to a change in stretch $\delta\overline{\lambda}(z)$ along the length in equilibrium; one would expect larger stretches ($\delta\overline{\lambda} > 0$) in regions where the cross-sectional area is smaller ($\delta A_i < 0$). The change in stretch can be computed from Eq. (8). To linear order in the perturbation, $\delta A_i(z)$, we find

$$\frac{\delta\overline{\lambda}}{\overline{\lambda}} = \frac{\overline{\sigma}}{\overline{\sigma} - \overline{E_P}}\frac{\delta A_i}{A_i}, \qquad \frac{\delta\overline{A}}{\overline{A}} = \frac{\overline{E_P}}{\overline{E_P} - \overline{\sigma}}\frac{\delta A_i}{A_i}. \tag{14}$$

As in the case of elastic perturbations, the amplitude of stretch (and hence the decrease in the area of cross-section)in regions with smaller initial cross-sectional areas diverges as the tangent stiffness $\overline{E_P}$ approaches $\overline{\sigma}$. In other words, the material fails by necking when this limit is approached, and there are no solutions for the case of a soft ECM (*i.e.* when $\overline{E_P} < \overline{\sigma}$).

2.3 Perturbations in contractility and parallel stiffness

If the initial density of cells and the ECM are not uniform, the contractility and hence the stall stress, σ_S^{max}, and the parallel stiffness, characterized by the the tangent parallel stiffness at zero strain E_P^0 in the neo-hookean relation, can vary along the length of the tissue. Denoting $\delta\sigma_S^{max}$ and δE_P^0 as the perturbations in these parameters, the variations in stretch and cross-sectional area can be derived from Eq. (8):

$$\frac{\delta\overline{\lambda}}{\overline{\lambda}} = -\frac{\delta\overline{A}}{\overline{A}} = -\frac{\delta\sigma_S^{max}}{\overline{E_P} - \overline{\sigma}} - \frac{\delta E_P^0}{E_P^0}\frac{\sigma_P}{\overline{E_P} - \overline{\sigma}}. \tag{15}$$

Again, as in the previous cases, we find that stretching and thinning diverge as $\overline{E_P}$ approaches $\overline{\sigma}$, and no physical solutions can be found for the case of a soft ECM (*i.e.* when $\overline{E_P} < \overline{\sigma}$), illustrating that the instability condition we have derived holds for a variety of perturbations.

2.4 Stability phase diagram

The condition for stability of the tissue $\overline{E_P} \geq \overline{\sigma}$ can also be written as

$$\frac{\overline{E_P}}{\sigma_S^{max}} \geq \frac{\overline{P}}{\sigma_S^{max} A_i}\overline{\lambda} \tag{16}$$

For incompressible neo-hookean materials, $\overline{P}$, $\overline{\lambda}$ and $\overline{E_P}$ can be solved from

$$\begin{aligned}
&\frac{1}{3}\frac{E_P^0}{\sigma_S^{max}}\left[\overline{\lambda}^2 - \frac{1}{\overline{\lambda}}\right] + 1 = \frac{\overline{P}}{\sigma_S^{max} A_i}\overline{\lambda} \\
&\frac{\overline{P}}{\sigma_S^{max} A_i} = \frac{1}{2}\frac{k_b L_i}{\sigma_S^{max} A_i}(1 - \overline{\lambda}) \\
&\frac{\overline{E_P}}{\sigma_S^{max}} = \frac{1}{3}\frac{E_P^0}{\sigma_S^{max}}\left[2\overline{\lambda}^2 + \frac{1}{\overline{\lambda}}\right]
\end{aligned} \tag{17}$$

where $\overline{P}/\sigma_S^{max} A_i$ is scaled tension, $k_b L_i/\sigma_S^{max} A_i$ is the scaled boundary stiffness and E_P^0/σ_S^{max} is the scaled parallel stiffness.

For small deformations ($|\ln\lambda| \ll 1$), the logarithmic strain is equal to the engineering strain ($\ln\lambda \approx \lambda - 1$), and Eq. (17) can be solved in closed form to obtain Eq. (3) of the main text,

$$\overline{\sigma} = \frac{\sigma_S^{max}}{1 + \frac{2E_P^0 A_i}{k_b L_i}}. \tag{18}$$

Eqs. (16) and (17) can be solved to obtain the phase diagram shown in Fig. 4E of the main text. The stretch along the phase boundary can be expressed as

$$\overline{\lambda} = 2\sqrt{\frac{\sigma_S^{max}}{E_P^0}}\cos\left(\frac{\pi}{3} + \frac{1}{3}\arctan\sqrt{\left(\frac{\sigma_S^{max}}{E_P^0}\right)^3 - 1}\right). \tag{19}$$

This expression for stretch can be used in the equation

$$\frac{k_b L_i}{\sigma_S^{max} A_i} = \frac{2(1 + 2\overline{\lambda}^3)}{\overline{\lambda}(1 - \overline{\lambda})(2 + \overline{\lambda}^3)} \tag{20}$$

to obtain the phase boundary shown in Fig. 4E of the main text. For $k_b L_i/\sigma_S^{max} A_i \to \infty$, the tissue is stable for $E_P^0/\sigma_S^{max} > 1$. For $k_b L_i/\sigma_S^{max} A_i < 4.545$ or $E_P^0/\sigma_S^{max} > 1$, the tissue is always stable.

2.5 Necking instability in special limiting cases

2.5.1 Infinitely series stiffness limit $\overline{E_c} \to \infty$ (2-parallel element model)

The 3-element model is same as 2-element model of Joanny and Prost [16] for infinitely series stiffness. The instability using 2-elment model can be directly derived in Eq. 13 as $\overline{E_c} \to \infty$,

$$\frac{\dot{\delta\lambda}(z,t)}{\delta\lambda(z,t)} = -\overline{E_C} K \dot{\epsilon}_A^{max} \frac{\overline{E_P} - \overline{\sigma}}{\overline{E_C} + \overline{E_P} - \overline{\sigma}} = -K\dot{\epsilon}_A^{max}(\overline{E_P} - \overline{\sigma}) \tag{21}$$

For 2-element model, tissue is stable as $K\dot{\epsilon}_A^{max}(\overline{E_P}-\overline{\sigma}) > 0$. Since the slope of the contractile strain vs stress curve $K > 0$, the stability criterion for 2-element model is $\overline{E_P} > \overline{\sigma}$. The stability criterion for 3-element mode is $(\overline{E_P} - \overline{\sigma})(\overline{E_C} + \overline{E_P} - \overline{\sigma}) > 0$. The parallel element is under compression $\overline{\sigma_P} < 0$ due to the active contraction. In the main text, we assume the series element is a hyperelastic material with $\overline{E_C} > \overline{\sigma_A} = \overline{\sigma} - \overline{\sigma_P}$, so the stability criterion becomes $\overline{E_P} > \overline{\sigma}$ for the 3-element model, which is same as that of the 2-element model. The series passive component $\overline{E_c}$ is therefore not essential to obtain the instability.

2.5.2 Free boundary conditions $\overline{\sigma} = 0$

$$\frac{\dot{\delta\lambda}(z,t)}{\delta\lambda(z,t)} = -\overline{E_C}K\dot{\epsilon}_A^{max}\frac{\overline{E_P} - \overline{\sigma}}{\overline{E_C} + \overline{E_P} - \overline{\sigma}} = -\overline{E_C}K\dot{\epsilon}_A^{max}\frac{\overline{E_P}}{\overline{E_C} + \overline{E_P}} < 0 \tag{22}$$

Unconstrained tissue is always stable, which can explain why unconstrained gels were found to be stable in Fig. 9C.

2.5.3 Activity is suppressed $\overline{\sigma_A} = 0$

If the activity is suppressed $\overline{\sigma_A} = 0$, the total stress can be expressed as the sum of active and parallel stress $\overline{\sigma} = \overline{\sigma_A} + \overline{\sigma_P}$,

$$\frac{\dot{\delta\lambda}(z,t)}{\delta\lambda(z,t)} = -\overline{E_C}K\dot{\epsilon}_A^{max}\frac{\overline{E_P} - \overline{\sigma}}{\overline{E_C} + \overline{E_P} - \overline{\sigma}} = -\overline{E_C}K\dot{\epsilon}_A^{max}\frac{\overline{E_P} - \overline{\sigma_P}}{\overline{E_C} + \overline{E_P} - \overline{\sigma_P}} \tag{23}$$

The stability criterion $\overline{E_P} > \overline{\sigma_P}$ is consistent with the classic Considère instability [17] for the passive parallel element.

2.5.4 For very soft parallel element $\overline{E_P} \to 0$

$$\frac{\dot{\delta\lambda}(z,t)}{\delta\lambda(z,t)} = -\overline{E_C}K\dot{\epsilon}_A^{max}\frac{\overline{E_P} - \overline{\sigma}}{\overline{E_C} + \overline{E_P} - \overline{\sigma}} = \overline{E_C}K\dot{\epsilon}_A^{max}\frac{\overline{\sigma}}{\overline{E_C} - \overline{\sigma}} > 0 \tag{24}$$

Tissue is unstable in the absence of parallel element, so the the 2-element model with the active and passive elements in series is always unstable.

2.5.5 For infinitely stiff parallel element $\overline{E_P} \to \infty$

$$\frac{\dot{\delta\lambda}(z,t)}{\delta\lambda(z,t)} = -\overline{E_C}K\dot{\epsilon}_A^{max}\frac{\overline{E_P} - \overline{\sigma}}{\overline{E_C} + \overline{E_P} - \overline{\sigma}} = -\overline{E_C}K\dot{\epsilon}_A^{max} < 0 \tag{25}$$

Tissue is stable for infinitely stiff parallel element. The parallel passive element (dense ECM) can make the tissue stable, which is consistent to our experimental observations for self assembled cardiac microtissues (Fig. 1 and the phase diagram in Fig. 4E of the main text).

3 Implementation of the constitutive laws using ABAQUS UMAT

All our simulations were performed in a finite deformation setting. The tissue was modeled using 3D eight-noded linear brick elements. For the fibroblast tissues in Fig. 2 of the main text, the

constraining pegs were modeled as rigid cylindrical surfaces. In the early stages of self assembly, the tissue fills the torus and the connecting rod and wraps around the pegs completely (refer to Fig. 2A of the main text). In our numerical simulations, we model the contact between the microtissue and the peg using a contact algorithm that guarantees that the surfaces of the peg and the tissue do not interpenetrate. The algorithm also allows for the tissue to retract from the surface of the peg in regions where the tensile stresses are large. The 3D constitutive relations (the hyperelastic constitutive law and Eq. (1) in the main text), the equilibrium condition, $\partial\sigma_{ij}/\partial x_j = 0$ and the boundary conditions constitute a well-posed boundary value problem. These equations are solved using the software package, ABAQUS, by formulating the 3D constitutive laws via the user defined subroutine UMAT [18]. The schematic shown in Fig. 5 shows the main steps involved in this implementation.

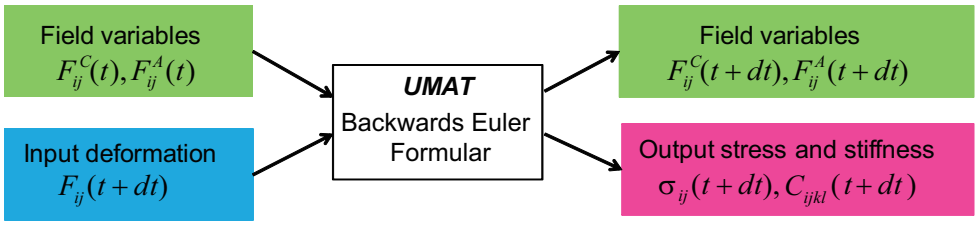

Figure 5: Schematic of UMAT implementation.

The backwards Euler discretization of the 3D constitutive law is solved using the Newton iteration in our UMAT implementation:

$$
\begin{aligned}
&F_{ij} = F_{ij}^P = F_{ik}^C F_{kj}^A, \\
&\sigma_{ij} = \sigma_{ij}^C + \sigma_{ij}^P = \sigma_{ij}^A + \sigma_{ij}^P, \\
&\sigma_{ij}^C = \frac{1}{J_C}\frac{\partial W_C}{\partial F_{ik}^C} F_{jk}^C, \\
&\sigma_{ij}^P = \frac{1}{J_P}\frac{\partial W_P}{\partial F_{ik}^P} F_{jk}^P, \\
&F_{ik}^C\left(\frac{F_{kn}^A - F_{kn}^A(t)}{dt}\overline{F}_{nl}^A\right)\overline{F}_{lj}^C = \frac{3}{2} S_{ij}^A \frac{\dot{\epsilon}_A^{max}}{\sigma_A}\Psi\left(\frac{\sigma_A}{\sigma_S^{max}}\right),
\end{aligned}
\tag{26}
$$

where the deformation gradients $\mathbf{F}$, $\mathbf{F}_A$, $\mathbf{F}_C$, $\mathbf{F}_P$ and Cauchy stresses $\boldsymbol{\sigma}$, $\boldsymbol{\sigma}_A$, $\boldsymbol{\sigma}_C$, $\boldsymbol{\sigma}_P$ at the end of each time increment should be determined (all quantities in the above equations correspond to time $t + \Delta t$, unless otherwise indicated). $J_C = \det\mathbf{F}_C$ and $J_P = \det\mathbf{F}_P$. $\mathbf{F}_C\overline{\mathbf{F}}_C{=}\mathbf{I}$ and $\mathbf{F}_A\overline{\mathbf{F}}_A{=}\mathbf{I}$, where $\mathbf{I}$ denotes the identity matrix.

4 Experiments on loop ended dogbone microtissues

Solid Works computer-aided design (CAD) software (Solid Works Corporation, Concord, MA) was used to design micromolds containing loop-ended dogbone-shaped recesses (Fig. 6). A ThermoJet1 rapid prototyping machine (3D Systems Corporation, Valencia, CA) was then used to generate wax prototypes of the micromolds. Polydimethylsiloxane (PDMS) (Sylguard 184, Dow Corning, Midland, MI) negatives of the micromolds were cast directly from the wax prototypes and sterilized via

autoclave. From these PDMS micromold negatives, we cast nonadhesive hydrogel micromolds consisting of 2% (w/v) agarose in phosphate-buffered saline (Ultrapure Agarose, Invitrogen, Carlsbad, CA). Loop-ended dogbone microtissues were formed by seeding suspensions of NHFs directly into the nonadhesive hydrogel micromolds. Prior to seeding, the NHFs were fluorescently labeled with CellTracker^{TM} Green CMFDA (Invitrogen, Eugene, Oregon). They were subsequently imaged via time-lapse fluorescent microscopy on a Carl Zeiss Axio Observer Z1 equipped with an AxioCam MRm camera (Carl Zeiss MicroImaging, Thornwood, NY) and an environmental chamber (37^oC, 10% CO_2).

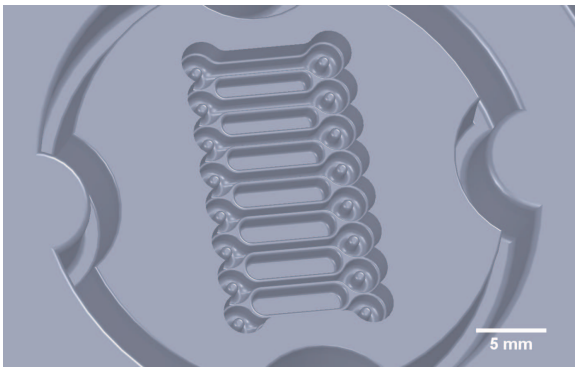

Figure 6: SolidWorks CAD model of micromold containing loop-ended dogbone-shaped recesses.

By analyzing the fluorescent time-lapse images, we were able to deduce the morphological changes that occur in the dogbone microtissues in all three spatial dimensions. The raw images demonstrated the morphological changes that occur in the x- and y-dimensions, and information on the z-dimension was ascertained via analysis of the fluorescence intensity of the tissue. Fluorescence intensity corresponds with cell density and hence thickness of the microtissue in the z-dimension. All fluorescence intensity measurements were taken from the same device and are reported in "Relative Fluorescence Units" (RFU).

Fluorescent images of the dogbone microtissues were analyzed using a combination of AxioVision (Rel. 4.8; Zeiss), Matlab (R2012b; MathWorks), and ImageJ (NIH, Bethesda, MD) softwares. Fluorescence profiles along lines crossing the dogbone microtissue at various positions were obtained using the 'Measure' function in Axiovision software. The resulting fluorescence profiles were analyzed by a user-defined Matlab function to find the length of dogbone microtissue and total fluorescence along the lines. It was noted that the microtissues would lose fluorescence throughout the course of the time-lapse due to photobleaching. Thus, a corrective index, which could be applied to fluorescence measurements of the microtissue, was calculated for each time point. This was done by first using ImageJ (NIH, Bethesda, MD) software to quantify the total fluorescence emanating from the entirety of the tissue at each time point. Briefly, ImageJ's 'Import'>'Image Sequence' function was first used to open the series of fluorescence images from a time-lapse of an individual microtissue within the software. Background fluorescence (i.e., the fluorescence of the hydrogel and stage) was then subtracted by applying the 'Subtract Background' function to all the images in the time-lapse series simultaneously. Next, the 'Polygon Selections' function was used to draw an outline around the dogbone microtissue, and the total fluorescence within the outline (i.e., the total microtissue fluorescence) was measured using ImageJ's 'Measure' function. The corrective index at

each time point was then calculated by dividing the total microtissue fluorescence at the time point by the total microtissue fluorescence at the initial time point. Corrected fluorescence values at the measured positions along the dogbone microtissue were obtained by dividing the original fluorescence values by the calculated corrective indices. Thus, we were able to determine a functionalized cross-sectional area at various positions along the rod of the dogbone microtissue by multiplying width and average fluorescence intensity at the respective position.

By assuming that the tissue was incompressible and comparing the functionalized cross-sectional area at individual time points to the functionalized cross-sectional area at the initial time point (Fig. 7), we could ascertain the strain evolution of the microtissue over time (Fig. 8). The strains deduced with this method are consistent with the strains measured by GFP labeling cells and measuring their lengths (Fig. 9A) [19], justifying the assumption that the cells deform in a nearly incompressible manner. Both methods show that cells at the failure points stretch to 30-50 times their original lengths. Furthermore, the observations of GFP labeled cells (Fig. 9B) confirm that they do not divide or migrate over the time scale of the experiments, which justifies the hyperelastic material model used to model the passive stiffness of the cells.

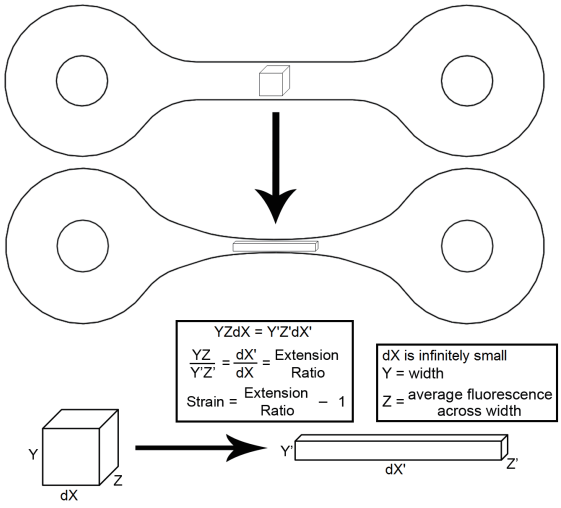

Figure 7: Schematic of strain calculation in dogbone microtissues.

After seeding in nonadhesive hydrogel micromolds, fibroblasts self-assembled into microtissues consisting of two toroids connected by a rod (Fig 8A for t=1hour). Fig. 8B-E depicts the temporal evolution of width, average fluorescence (i.e., height), functionalized area and strain at a point near the center. As expected, the decrease in width is accompanied by an increase in strain.

We found the maximum stretch can reach a factor of 50 (Fig. 8E), which is consistent with the elongation factor of 30 observed by GFP labeling cells (Fig. 9A) [19]. For self-assembling unconstrained rods of similar size, no dramatic cell elongation and microtissue failure was observed (Fig. 9A and 9C). We also used rat Hepatocyte (H35) tissues, which are much less contractile than the NHFs, and repeated the above experiments. No necking or failure was observed in H35 microtissues for over a week (Fig 10). Furthermore, failure was significantly inhibited by Y-27632 and blebbistatin in NHF tissues, although Y-27632-treated samples were significantly more inhibited

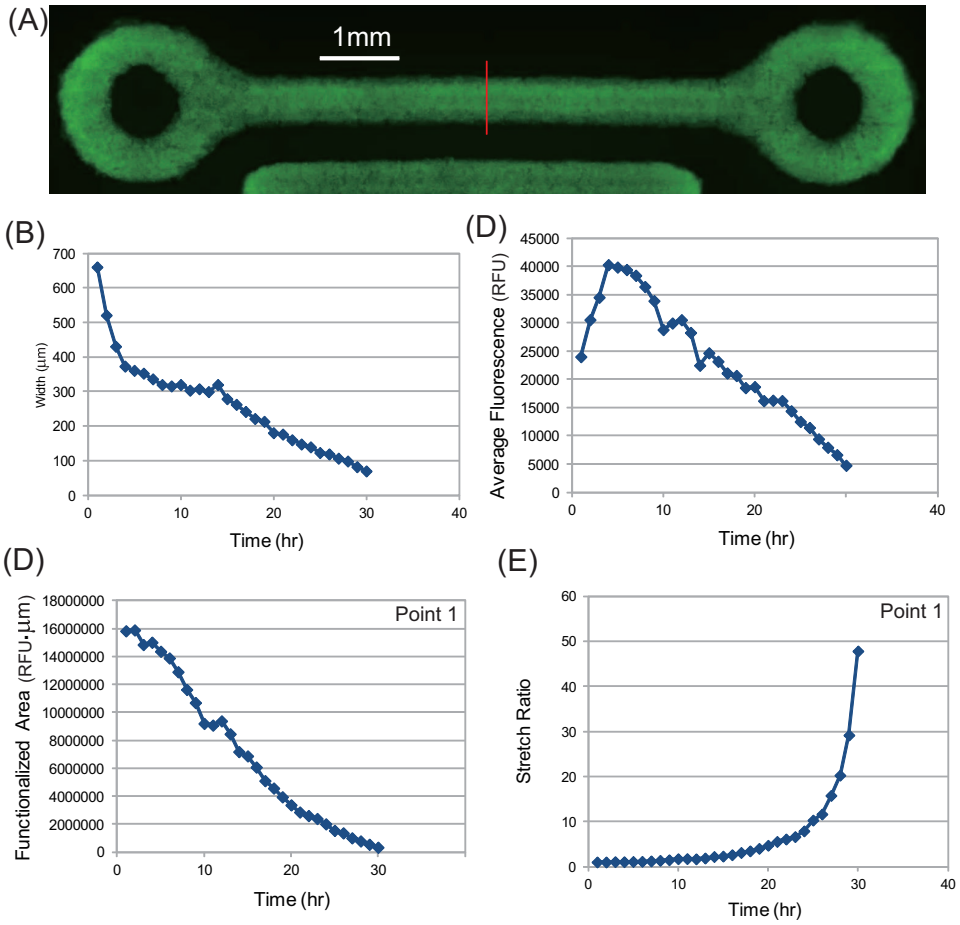

Figure 8: (A) Loop-ended dogbone shaped NHF microtissue at t=1hour. (B)-(E) Temporal evolutions of width, average fluorescence, functionalized cross-sectional area and stretch ratio near the center of the dogbone microtissue (labeled by red line in top panel of Fig. 2(A) of the main text).

than blebbistatin-treated samples [19]. These experimental results clearly confirm our predictions that actomyosin contractility leads to instability and failure of constrained microtissues.

5 Fitting curves using a random search algorithm

The stability and morphological evolution of microtissues are determined by the scaled tangent series stiffness at zero strain, E_C^0/σ_S^{max}, the scaled tangent parallel stiffness at zero strain, E_P^0/σ_S^{max}, and the scaled boundary stiffness, $k_b L_i/\sigma_A^{max} A_i$. These parameters were obtained by fitting six sets of measured tissue force and area vs time curves (Fig. 1C-D of the main text) to actual experimental results using a random search algorithm [20]. For each group of parameters, the simulation curves were generated and compared with the experimental data. The optimized parameters were obtained by minimizing the sum of squared residuals (defined as the difference between the experimental and simulation data). A similar procedure was used to obtain the fits for the dogbone NHF tissue (Fig. 11).

6 Definition of the reference configuration

While the reference configuration for a collection of cells that organize to form a tissue is difficult to define in general (i.e. specify the configuration $\mathbf{X}$ defined in the main text), in both of our experiments this can be done in a unique and unambiguous manner. In the case of CMTs, the reference is the configuration of tissue just prior to the deflection of the cantilever. The defection of the cantilever allows us to uniquely measure strains both in the axial and transverse directions (from the change in width of the tissue). To demonstrate the existence of a reference configuration, we have developed a microrobotic platform capable of performing automated mechanical characterization of microtissues as they grow. The system employs a microgripper, a high-precision three-axis micromanipulator with position feedback (5 nm resolution) and a customuser interface for the guiding of the automated measurement process. We integrated the system with an inverted fluorescent microscope and recorded images of microtissues during mechanical loading (Fig. 13).

As we experimentally and computationally demonstrated in Fig. 1 of the main text, for relatively high collagen concentration and low cantilever stiffness, the cross sectional area and the static force on microtissues remain constant over days once they reach a steady state value. We measured the static force and passive elasticity of microtissues at different time points of growth, before and after abolishing the myosin activity (Fig. 14).

To abolish the myosin activity, the microtissues were treated with 100 μM Blebbistatin (Sigma-Aldrich, St. Louis, MO). Fig. 15 shows representative stress-strain curves of microtissues on day2 and day4 before and after abolishing myosin activity. The results showed that, after the microtissues were fully formed, the change in passive elasticity, measured by stretching the tissue with the microgripper, was negligible over the course of experiments (Fig. 14B). The cross sectional area and also did not show any variation during the course of growth. The results for the passive elasticity we find in Fig. 14 (modulus 15 kPa) is in agreement with those reported [21], although that work did not consider stiffness at different stages of growth. The data is also in excellent agreement with independent estimates obtained by fitting our model to the deflection of the posts and the morphology of the tissue, confirming that the validity of the assumptions made in our model.

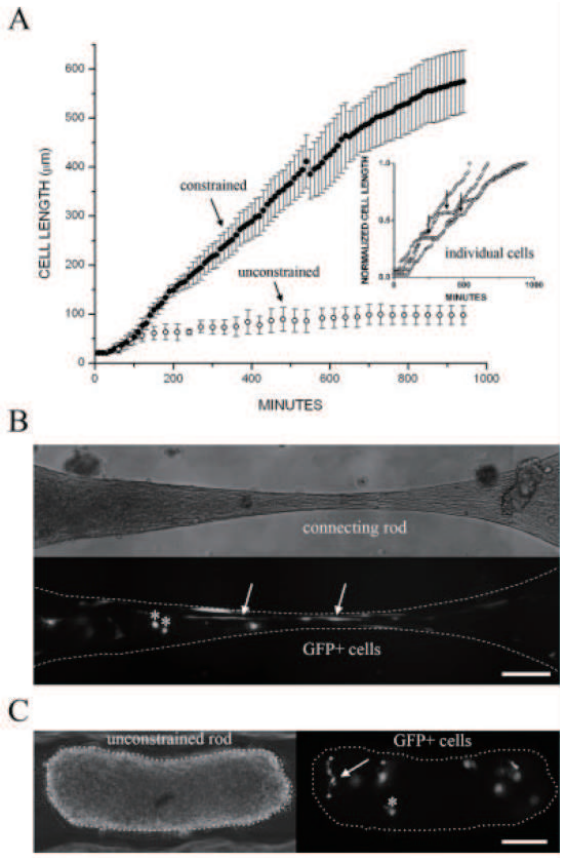

Figure 9: Lengths of cells in constrained (closed circles) and unconstrained (open circles) rods were measured over time (A) [19]. Average cell length increased linearly, but some cells had periods of stagnancy (inset, arrows). Only cells that elongated beyond 200 μm in constrained rods were measured. Not all cells elongated in the connecting rod. NHFs in unconstrained rods rarely elongated beyond 100 μm and only cells that elongated beyond 50 μm were measured. Phase and fluorescence microscopy images for constrained (B) and unconstrained microtissues (C) show rounded (*) and elongated cells (arrows). Scale bars 150 μm. These images are reproduced from [19] with the authors's permission.

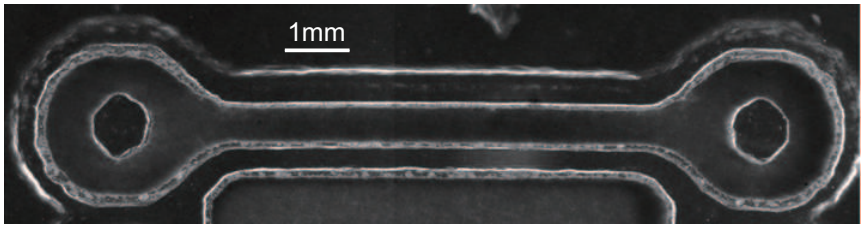

Figure 10: H35 dogbone shaped microtissues did not develop tension or fail and were found to be stable. The figure shows the morphology one week after initial seeding.

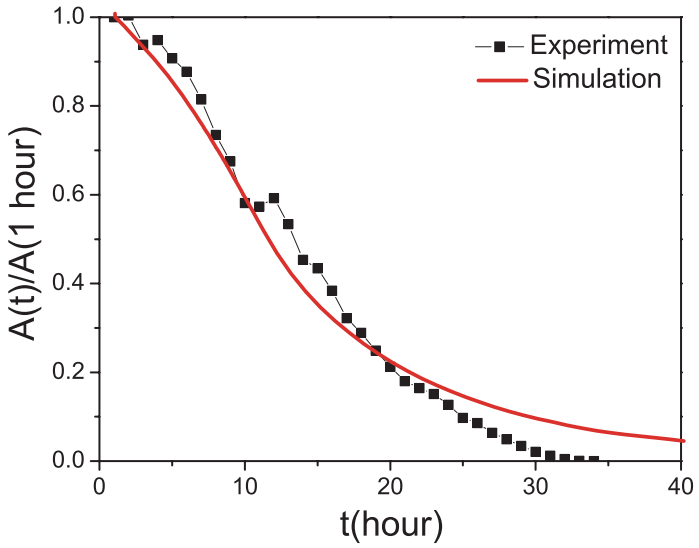

Figure 11: Evolution of cross-sectional area near the center of NHF dogbone microtissue (labeled by red line in top panel of Fig. 2(A) of the main text) from simulations (red line) and experiment (black squares).

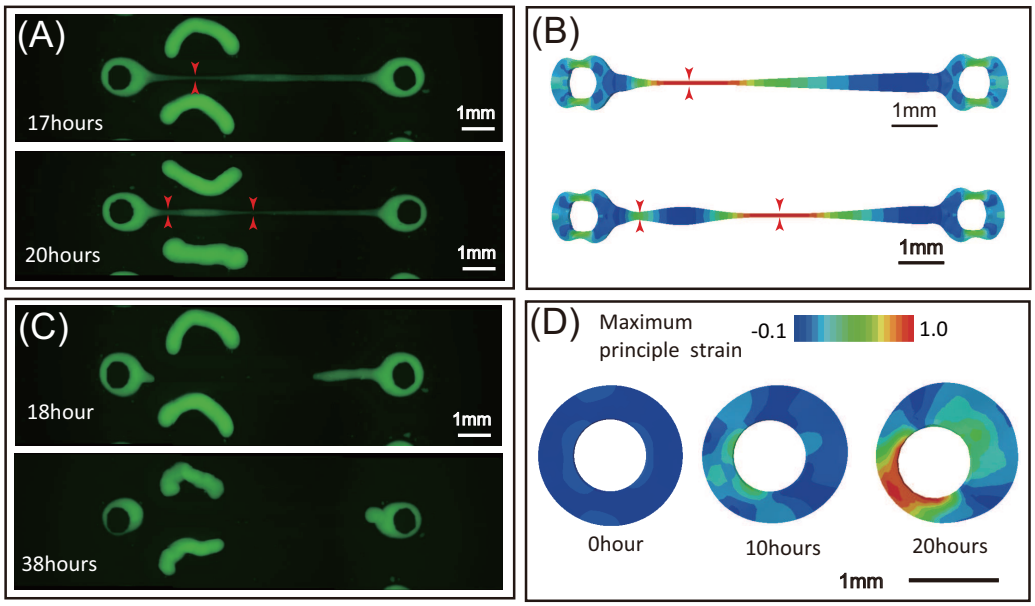

Figure 12: (A,B) Observations and simulations of asymmetric failure (failure away from the midpoint of the connecting rod) and failure at two points. (C) Failure of tori around the pegs after failure of the connecting rod. (D) FEM simulations of the shape evolution of toroid shaped microtissues.

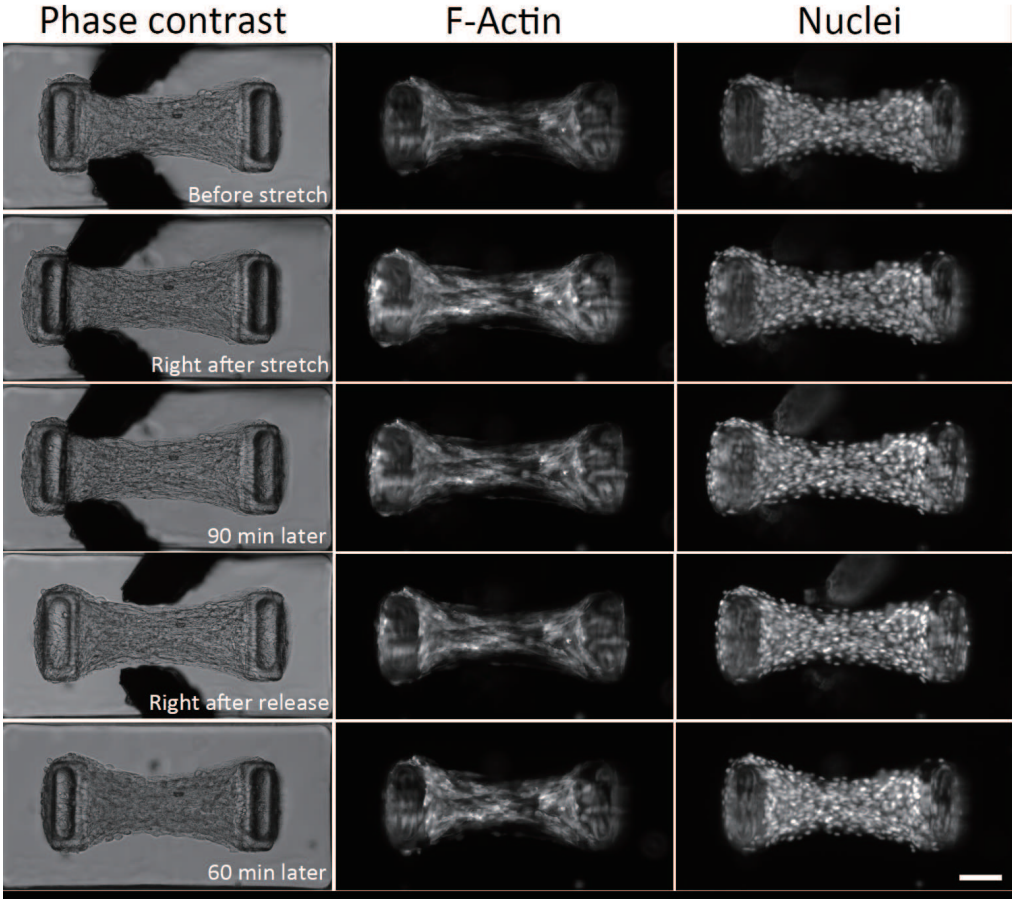

Figure 13: Phase contrast images and accompanying fluorescence images of F-actin and nuclei of microtissues before, during and after tensile loading. Compared to the state right after stretch, microtissues slowly elongated further in time. Immediately after the tension was removed, the microtissues were longer than their initial length before stretch and they eventually relax back to their original shape in time. Scale bar is 100 μm.

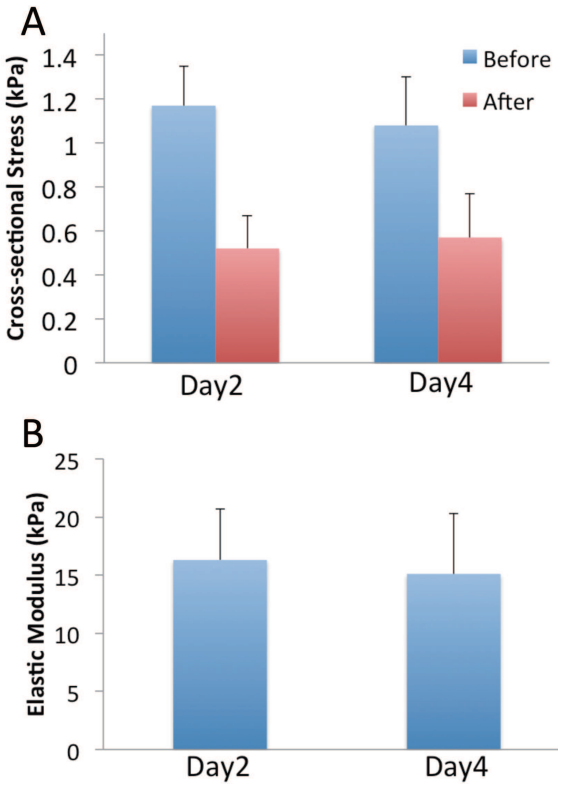

Figure 14: Comparisons of cross-sectional stress (A), and elastic modulus (B) of pharmacologically treated microtissues (with Blebbistatin) and untreated microtissues on day2 and day4. 10 samples were analyzed for both cases. All data are presented as Mean±S.D.

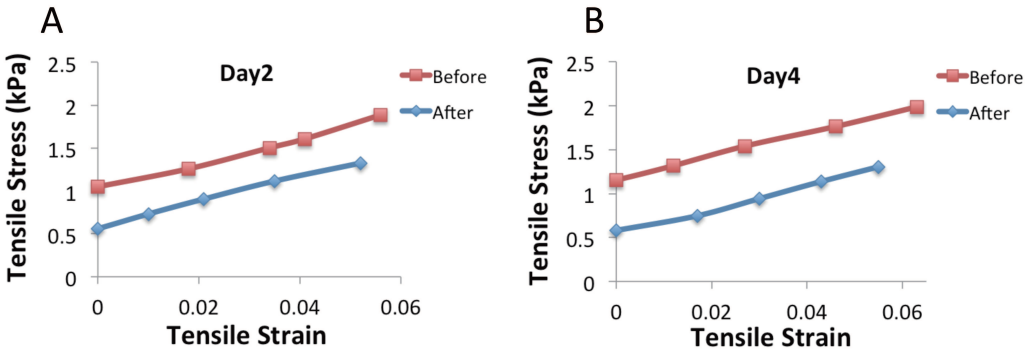

Figure 15: Representative stress-strain curves of microtissues. The tissue elastic modulus E is reported as the slope of such curves.

We also applied tensile stretch for 1-5 hours and the microtissues (with and without myosin activity) relaxed back eventually to their original shape after the force is removed (Fig. 13). The microtissues were longer and thinner compared to their initial dimensions right after loading (Fig. 13). We also performed live fluorescence imaging and visualized actin cytoskeleton and nuclei of embedded cells during the loading experiments. Half of the cells were transfected with LifeAct-GFP to label F-actin and all the nuclei were stained with Hoechst. Comparison between phase-contrast images and fluorescent live images showed that encapsulated cells deformed with the collagen matrix as a coherent body and the mechanical stimulation was fully transferred to the cells. We did not observe any detectable change in the distribution of actin filaments or nuclei after tensile loading was removed and when the tissue relaxed back (Fig. 13). All tested microtissues regained their original passive stress after the loads were removed.

In summary, we have convincingly demonstrated that (a) the passive elasticity of the tissue remains the same at different time points of growth (Fig. 14) and (b) the tissues maintains coherence over long periods of force application and relax back to the original configuration after force is removed (Fig. 13). This unambiguously proves the existence of a reference configuration.

7 Staining for actin and collagen

NHF dogbones were self-assembled for 16 hours and fixed with 4% paraformaldehyde. Collagen I was immunostained with a monoclonal antibody to collagen I (Abcam, Cambridge MA) and a Cy3 goat anti-mouse IgG secondary (Jackson ImmunoResearch Laboratories, West Grove, PA). Following the immuno-staining of the microtissues, the actin was labeled with Oregon Green®448 phalloidin (Life Technologies, Grand Island, NY) and the nuclei with DAPI (4′,6-Diamidino-2-Phenylindole, Dihydrochloride; Life Technologies, Grand Island, NY). Confocal images were captured with a Zeiss LSM 510 confocal microscope (Carl Zeiss MicroImaging, Thornwood, NY, USA).

NHF dogbones at 16 hours were stained for actin fibers (phalloidin), collagen type I (antibody), nuclei (DAPI) and imaged using confocal microscopy (Fig. 16). The stain for nuclei shows that the cells in the 3D microtissue are very densely packed and the majority of cells are aligned along the long axis of the microtissue as shown by the orientation of the long axis of the nuclei. The stain for actin shows that stress fibers are abundant and aligned in the direction of the long axis of the microtissue. Further, the majority of fibers are located at the periphery of cells. The immuno-stain for collagen type I is diffuse, punctuate and not nearly as aligned as actin, consistent with a more cytoplasmic and unorganized distribution. Certainly ECM such as collagen type I is present, but at this early time point (16 hours of self-assembly) the prominence and orientation of the actin stress fibers suggests that they perform a more critical role than the unorganized collagen. Further, in a prior publication we showed that at this early time point NHFs in a densely packed spherical microtissue are coupled to one another via gap junctions [22].

In the case of CMTs, we performed immuno-staining of collagen and we observed that it was compacted and aligned along the long axis (Fig. 17). Also, in order to determine if CMTs behave as a contiguous tissue, we previously examined whether electrical signals conduct across the engineered tissues by exposing constructs to a fluorescence-based calcium indicator and taking fluorescence images at 30 Hz [13]. We observed synchronized calcium release across the entire microtissue. This synchronized calcium release was observed with coherent beating and the maturation of the CMTs after approximately 3 days of culture, and was associated with the development of sarcomeric structures and cell-cell contacts. We also performed immuno-staining of Troponin-T in CMTs after 7 days of culture (Fig. 18). As troponin is a component of thin filaments (along

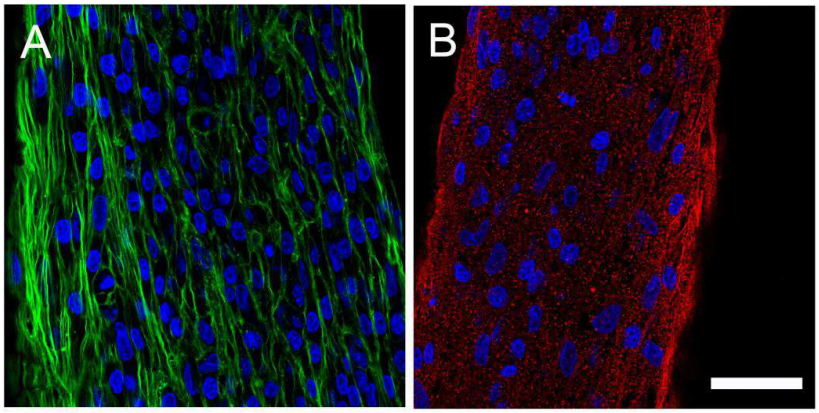

Figure 16: Self-assembled NHF dogbone microtissues are dominated by highly aligned actin filaments. NHF dogbones were fixed after 16 hours of self-assembly and were stained for actin fibers (phalloidin, green), collagen type I (antibody, red), nuclei (DAPI, blue) and imaged using confocal microscopy. The stain for nuclei and actin (A) shows that the cells in the dogbone are densely packed and the majority of cells are aligned along the long axis of the microtissue as shown by the orientation of the major axis of the nuclei. The stain for actin shows that stress fibers are abundant and highly aligned along the long axis of the microtissue. Further, the majority of actin fibers are located at the periphery of cells. The immuno-stain for collagen type I (B) is diffuse, punctuate and not nearly as aligned as actin.

with actin and tropomyosin), it is a good indicator of the spatial organization of the cytoskeleton of cardiomyocytes. We observed longitudinally aligned and elongated thin filaments, along with a well-developed parallel cross-striation pattern, consistent with sarcomeric structures. These parallel cross-striations highlight the very directional contractions of CMTs along the axis between the two cantilevers.

8 Cell viability and nutrient supply

We have seen little if any cell division or cell death for NHFs in micro-molds of various geometries. In a prior publication, we showedthat NHF spheroids were viable for as long 2 weeks [23] and that the volume of a toroid of NHFs does not change (increase or decrease) during the 12 hour period in which cells self-assemble a toroid that moves up a cone [24]. The micro-molded agarose gels into which the NHFs are seeded are pre-equilibrated with cell culture medium. These hydrogel micro-molds ensure that all sides of the 3D microtissue have access to the nutrients of cell culture medium. Since the experimental timeframe is relatively short (<40 hours) there is no need to change the culture medium.

By using a live/dead cell viability assay (Invitrogen), we estimated cell viability over time in the CMTs. The average normalized ratio of living cells (i.e. the percentage of living cells at one point divided by the percentage of living cells right after seeding) after 7 days of culture was 73±20%, statistically similar to the viability at day 1 (81±9%). As described in the Materials and

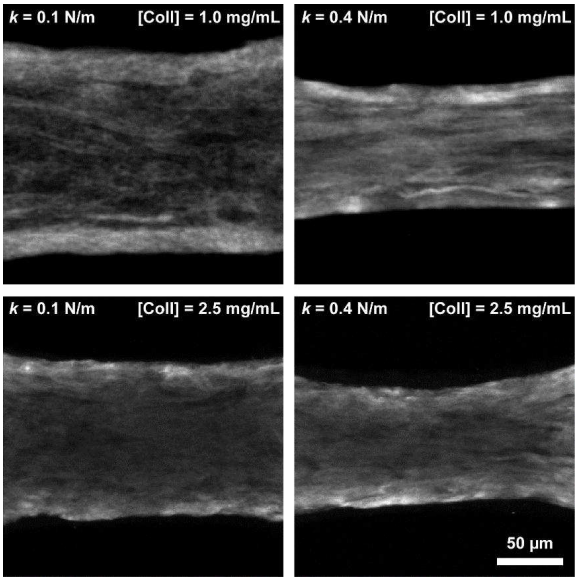

Figure 17: Representative top down views for CMTs showing collagen fibers after 48 hours of assembly.

Methods chapter, nutrients are directly presented in the cell culture medium. Cell culture medium was changed every day. Moreover, the small dimensions of the microtissue constructs allow for rapid penetration of soluble effectors into the constructs in absence of substantial diffusion barriers. Indeed, for simple diffusion (i.e., that governed by Fick's 2nd Law) the time required for diffusion of soluble factors scales with the thickness of the construct squared; therefore, concentration gradients in microtissues (thickness < 100 μm) should equilibrate 100 times faster than those in bulk gels (thickness 1 mm). To illustrate the experimental relevance of this effect, we previously showed that both 3D microtissues and single cells in 2D increased or decreased contractile forces within 5-10 min of treatment with lysophosphatidic acid (LPA), a known stimulant for myosin activity, or with blebbistatin, a myosin ATPase inhibitor, respectively [25].

9 Failure of the toroidal ends of the dogbones

It is noteworthy that our simulations also predict thinning and failure of the tissue surrounding the constraining pegs once the stress in the connecting rod relaxes as it thins and fails. In this case, hoop stresses build as the toroid shaped tissue contracts around the pegs. We find that small perturbations in the cross-section of the toroid lead to larger (tensile) hoop stresses in regions where the width of the tissue is smaller than the surroundings. The hoop stresses in regions distal and diametrically opposite to the thinned regions are compressive, causing thickening of these areas. This effect is clearly seen in the experiments (Fig. 12C) and in the simulations we have carried out with a toroid-shaped tissue (Fig. 12D). These observations confirm that necking instability in constrained tissues is a general phenomenon that does not depend on the way the constraints are applied.

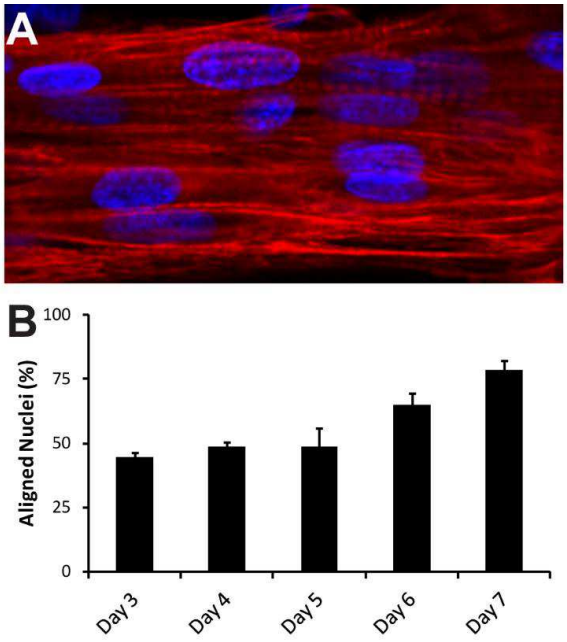

Figure 18: Structural properties of CMTs constructed in 0.5 mg/mL fibrin and 1.0 mg/mL collagen gels and tethered to rigid (k=0.45 mN/mm) cantilevers. (A) Immunostaining of troponin-T (red) and nuclei (blue) in a representative CMT at day 7. (B) Percentage of aligned nuclei ($angle < 20^o$). Data from (B) are the average of 6 CMTs±SEM.

Table 1: Major symbols and definitions

Symbol	Definition
$\boldsymbol{\sigma}$	Total stress tensor
$\boldsymbol{\sigma}_C$	Passive series stress tensor
$\boldsymbol{\sigma}_P$	Passive parallel stress tensor
$\boldsymbol{\sigma}_A$	Active stress tensor experienced by the actomyosin system
$\mathbf{S}_A$	Active stress deviator tensor
$\mathbf{F}$	Total deformation gradient tensor
$\mathbf{F}_C$	Deformation gradient tensor of the series element
$\mathbf{F}_P$	Deformation gradient tensor of the parallel element
$\mathbf{F}_A$	Deformation gradient tensor due to actomyosin activity
$\mathbf{D}_A$	Active deformation rate tensor
W_C	Strain energy function of the series element
W_P	Strain energy function of the parallel element
σ_S^{max}	Maximum values of the stall stress
$\dot{\epsilon}_A^{max}$	Maximum values of the contractile strain rate
σ_A	3D Equivalent active deviatoric stress
A_i	Initial uniform cross-sectional area of the tissue
L_i	Initial distance between the flexible posts
k_b	Stiffness of the flexible posts
σ	Total stress for uniaxial deformation
$\overline{\sigma}$	Total stress for uniaxial deformation in equilibrium
σ_C	Passive series stress for uniaxial deformation
σ_P	Passive parallel stress for uniaxial deformation
σ_A	Active stress experienced by the actomyosin system for uniaxial deformation
λ	Stretch ratio of the tissue
$\overline{\lambda}$	Stretch ratio of the tissue in equilibrium
$\dot{\lambda}$	Stretch rate of the tissue
$\dot{\epsilon}_A$	Active contraction rate
σ_S	Stall stress
$\dot{\epsilon}_A^{free}$	Active contraction rate in the absence of applied stresses
A	Cross-sectional area of the tissue
$\overline{A}$	Cross-sectional area of the tissue in equilibrium
P	Tension of the tissue
$\overline{P}$	Tension of the tissue in equilibrium
E_C	Tangent series stiffness
E_C^0	Tangent series stiffness at zero strain
$\overline{E_C}$	Tangent series stiffness in equilibrium
E_P	Tangent parallel stiffness
E_P^0	Tangent parallel stiffness at zero strain
$\overline{E_P}$	Tangent parallel stiffness in equilibrium
K	Slope of the strain rate vs. stretch curve at the stall point
η	Ratio of current to maximum levels for both stall stress and contraction rates
k_f	Formation rate of stress fibers
k_d	Dissociation rate of stress fibers

References

[1] A.V. Hill, *The heat of shortening and the dynamic constants of muscle*, Proc R Soc Lond B, 126 (1938), pp. 136–195

[2] M. Yoshigi, L.M. Hoffman, C.C. Jensen, H.J. Yost, and M.C. Beckerle, *Mechanical force mobilizes zyxin from focal adhesions to actin filaments and regulates cytoskeletal reinforcement*, J Cell Biol, 171 (2005), pp. 209–215

[3] K. Kurpinski, J. Chu, C. Hashi, and S. Li., *Anisotropic mechanosensing by mesenchymal stem cells*, Proc Natl Acad Sci, 103 (2006), pp. 16095–16100

[4] S. Jungbauer, H. Gao, J.P. Spatz, and R. Kemkemer, *Two characteristic regimes in frequency-dependent dynamic reorientation of fibroblasts on cyclically stretched substrates*, Biophys J, 95 (2008), pp. 3470–3478

[5] S. Thomopoulos, G,M. Fomovsky and J.W. Holmes, *The development of structural and mechanical anisotropy in fibroblast populated collagen gels*, J Biomech Eng, 127 (2005), pp. 742–750

[6] D. Mitrossilis, et al., *Single-cell response to stiffness exhibits muscle-like behavior*, Proc Natl Acad Sci USA, 106 (2009), pp. 18243–18248.

[7] K. Burridge, M. Chrzanowska-Wodnicka, *Focal adhesions, contractility, and signaling*, Annu Rev Cell Dev Biol, 12 (1996), pp. 463–518.

[8] K. Mochitate, P. Pawelek, F. Grinnell, *Stress relaxation of contracted collagen gels: Disruption of actin filament bundles, release of cell surface fibronectin, and down-regulation of DNA and protein synthesis*, Exp Cell Res, 193 (1991), pp. 198–207.

[9] F. Grinnell, *Fibroblasts, myofibroblasts, and wound contraction*, J Cell Biol, 124 (1994), pp. 401–404.

[10] R.P. Franke, et al., *Induction of human vascular endothelial stress fibres by fluid shear stress*, Nature, 307 (1984), pp. 648–649

[11] M. Ghibaudo, et al. *Traction forces and rigidity sensing regulate cell functions*, Soft Matter, 4 (2008), pp. 1836–1843

[12] V.S. Deshpande, R.M. McMeeking, and A.G. Evans, *A bio-chemo-mechanical model for cell contractility*, Proc Nat Acad Sci USA, 103 (2006), pp. 14015–14020.

[13] T. Boudou et al., *A Microfabricated Platform to Measure and Manipulate the Mechanics of Engineered Cardiac Microtissues*, Tissue Eng Part A, 18 (2012), pp. 910–919.

[14] J.W. Hutchinson, and H. Obrecht, *Tensile instabilities in strain-rate dependent materials*, Fracture, 1 (1977), pp. 101–116.

[15] J.W. Hutchinson, and K.W. Neale, *Influence of strain-rate sensitivity on necking under uniaxial tension*, Acta Metall, 25 (1977), pp. 839–846.

[16] J.F. Joanny, and J. Prost, *Active gels as a description of the actin-myosin cytoskeleton*, HFSP J, 3 (2009), pp. 94–104.

[17] A. Considère, Annales des Ponts et Chaussées, 9 (1885), pp. 574–775.

[18] ABAQUS Manual, Dassault Systemes, Providence, RI, Version 6.10, 2010

[19] D.M. Dean, A.P. Rago, and J.R. Morgan, *Fibroblast elongation and dendritic extensions in constrained versus unconstrained microtissues*, Cell Motil Cytoskeleton, 66 (2009), pp. 129–141.

[20] J. Bergstra and Y. Bengio, *Random search for hyper-parameter optimization*, J Mach Learn Res, 13 (2012), pp. 281–305.

[21] R.G. Zhao, T. Boudou, W.G. Wang, C.S. Chen, and D.H. Reich, *Decoupling cell and matrix mechanics in engineered microtissues using magnetically actuated microcantilevers*, Adv Mater 25 (2013), pp. 1699-1705.

[22] B. Bao, J. Jiang, T. Yanase, Y. Nishi, J.R. Morgan, *Connexon-mediated cell adhesion drives microtissue self-assembly*, FASEB J, 25 (2011), pp. 255–264.

[23] A.P. Napolitano, P. Chai, D.M. Dean and J.R. Morgan, *Dynamics of the self-assembly of complex cellular aggregates on micromolded nonadhesive hydrogels*, Tissue Eng, 13 (2007), pp. 2087–2094.

[24] J. Youssef, A.K. Nurse, L.B. Freund, and J.R. Morgan, *Quantification of the forces driving self-assembly of three-dimensional microtissues*, Proc Natl Acad Sci USA, 108 (2011), pp. 6993-6998.

[25] W.R. Legant, et al., *Microfabricated tissue gauges to measure and manipulate forces from 3D microtissues*, Proc Natl Acad Sci USA, 106 (2009), pp. 10097–10102.